# Electromagnetic Calorimeter for the Heavy Photon Search Experiment at Jefferson Lab

**Emma Buchanan**

A Thesis presented for the degree of
Master of Science


Nuclear Physics Experimental Research Group
School of Physics & Astronomy
University of Glasgow
Scotland

November 2014

## Abstract

The Heavy Photon Search Experiment (HPS) seeks to detect a hypothesised hidden sector boson, the A', predicted to be produced in dark matter decay or annihilation. Theories suggest that the A' couples weakly to electric charge through kinetic mixing, allowing it, as a result, to decay to Standard Matter (SM) lepton pairs [1], which may explain the electron and positron excess recently observed in cosmic rays [2], [3]. Measuring the lepton pair decay of the A' could lead to indirect detection of dark matter. The HPS experiment is a fixed target experiment that will utilize the electron beam produced at the Thomas Jefferson National Accelerator Facility (Jefferson Lab) [4]. The detector set-up includes a silicon vertex tracker (SVT) and an Electromagnetic Calorimeter (ECal). The ECal will provide the trigger and detect $e^+e^-$ pairs and its construction and testing forms the focus of this thesis.

The ECal consists of 442 $PbWO_4$ tapered crystals with a length 16 cm and a 1.6x1.6 $cm^2$ cross-section, stacked into a rectangular array and are coupled to Large Area APDs and corresponding pre-amplifiers. Supplementary to the ECal is a Light Monitoring System (LMS) consisting of bi-coloured LEDs that will monitor changes in APD gain and crystal transparency due to radiation damage.

Before construction of the ECal each of the components were required to be individually tested to determine a number of different characteristics. Irradiation tests were performed on $PbWO_4$ ECal crystals and, as a comparison, one grown by a different manufacturer to determine their radiation hardness. A technique for annealing the radiation damage by optical bleaching, which involves injecting light of various wavelengths into the crystal, was tested using the blue LED from the LMS as a potential candidate [5]. The light yield dependence on temperature was also measured for one of the $PbWO_4$ crystal types.

Each APD was individually tested to determine if they functioned correctly and within the requirements of the experiment, then arranged into groups of similar gain at chosen applied voltages, for connection to High Voltage (HV) supplies.

Each bi-coloured LED was also tested to determine if they functioned within the specifications of the experiment; including their signal quality at high frequency and

their radiation hardness.

The HPS crystals were recycled from a previous Jefferson Lab detector, the Inner Calorimeter from CLAS [6], which needed to be dismantled and reconditioned using various removal and cleaning techniques. The HPS ECal was then constructed in a new formation using a combination of different gluing and construction techniques, and initial functionality tests were performed.

# Declaration

The work in this thesis is based on research carried out at the Nuclear Physics Experimental Research Group, School of Physics & Astronomy, University of Glasgow, Scotland. No part of this thesis has been submitted elsewhere for any other degree or qualification and is all my own work unless referenced to the contrary in the text.

# Acknowledgements

Thanks to the Glasgow Nuclear Group for giving me this opportunity and guidance throughout the year. Special thanks to Daria for being a great supervisor. Also, I wouldn't have survived without the company of the other students in the group, so thanks for fun and distractions. Danke schön, to the "HPS support group"; Stuart, Luca, Gabriel and Holly for their continuous support and entertainment over the past year. Finally, I would like to thank my parents, Irene and Gerry for providing the financial support for this degree and to the rest of my family for their support and encouragement.

# Contents

# List of Figures

# List of Tables

# Chapter 1

# Dark Matter and the Heavy Photon

## 1.1 Dark Matter

Observations made in the 1930s first hinted that there may be more mass in the Universe than previous thought. Scientist Fritz Zwicky observed the velocity distributions of galaxies within the Coma cluster. From this he calculated that the Coma cluster was 400 times heavier than mass estimates for luminous matter [7]. This was later supported by studies of rotational curves of spiral galaxies in the 1970s. A rotational curve is a plot of a galaxy's rotational velocity as a function of increasing radius. The rotational velocity can be determined by measuring the Doppler shifts and is expected to steadily decrease for stars further away from the centre of the galaxy (Newtons law of gravity). However in reality the rotation curve remains constant as the radius from the galactic centre increases, see Figure 1.1. Therefore there must be additional unseen mass that surrounds the galaxy, often referred to as a dark matter halo [8].

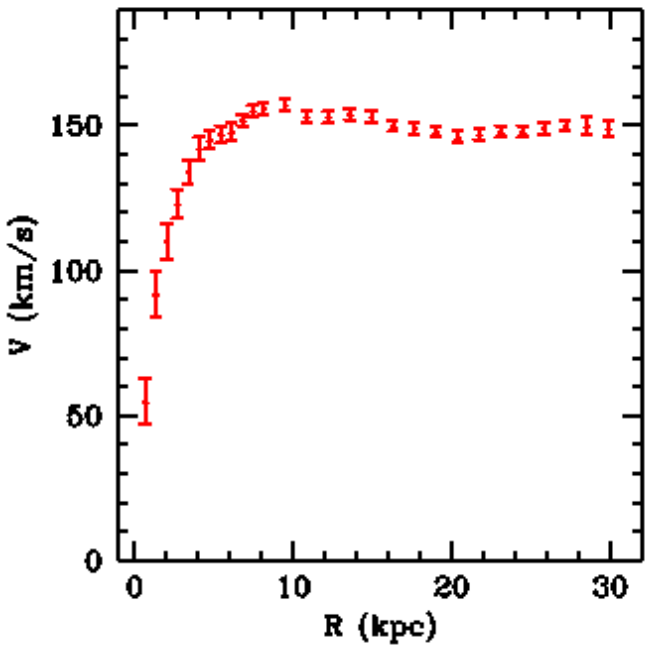


Figure 1.1: The rotation curve of spiral galaxy NGC3198 represents the measured rotational velocity using the Doppler shift of the galaxy with increasing radius from the galactic centre.

A leading cosmological model, Lambda Cold Dark Matter (ΛCDM), predicts that dark matter makes up 27% of the energy density of the Universe, with the rest of the density accounted for by Standard Model matter (5%) and dark energy (68%) [17]. There exist many proposed particle candidates which try to explain the dark matter component. The most widely researched being the WIMPs (Weakly Interacting Massive Particles) [11], the neutralino [9] and the gravitino [10].

Other less known dark matter candidates do exist, including the heavy photon (A') which is a new hypothesised gauge boson thought to be produced in dark matter decay or annihilation. A' is predicted to have a weak coupling to Standard Model matter allowing lepton pairs to be a decay product of A' [1], [11]. Measuring the produced leptons could lead to indirect detection of dark matter and may explain excess positrons and electrons recently measured in cosmic rays [2], [3]. One group searching for A' is the Heavy Photon Search (HPS) experiment which is a fixed target experiment designed to identify A' on the basis of their decay to $e^+e^-$ pairs [4].

## 1.2 Theoretical Motivations for A'

Recent theories attempting to describe dark matter interactions suggest that a new albelian U(1) gauge boson (A') exists which could couple to dark matter and mediate its interactions, much like the electromagnetic photon and Standard Model matter. The A', sometimes referred to as the dark photon or hidden sector photon, is also predicted to have a weak coupling to electrically charged particles by kinetically mixing with our own Standard Model photon. This can be represented as an extension to the Standard Model Lagrangian, $\mathcal{L}_{SM}$:

$$\mathcal{L} = \mathcal{L}_{SM} + \frac{\epsilon}{2} F^{Y,\mu\nu} F'_{\mu\nu} + \frac{1}{4} F'^{\mu\nu} F'_{\mu\nu} + m^2{}_{A'} A'^{\mu} A'_{\mu} \tag{1.1}$$

The $\frac{\epsilon}{2} F^{Y,\mu\nu} F'_{\mu\nu}$ term represents a kinetic mixing operator where an electromagnetic photon mixes with an A' boson [12]. The mixing is through interactions of massive fields inducing small couplings to electric charge. $F_{\mu\nu}$ describes the electromagnetic tensor, $A'_{\mu}$ is the heavy photon vector field and $m_{A'}$ is the mass of the heavy photon. A mixing parameter $\epsilon$ describes the strength of coupling of A' with a photon. It is often denoted as $\epsilon^2 = \frac{\alpha'}{\alpha}$ which is the ratio of the dark and Standard Matter electromagnetic couplings and has a natural scale, emergent from the theory, of $\backsim 10^{-8} - 10^{-2}$ [12]. Figure 1.2 helps illustrate the kinetic mixing interaction. The A' coupling to electrons is $\epsilon \cdot$e and the mass of $\mathrm{m}_{A'}$ is much greater than the mass of the electron $\mathrm{m}_e$. The reader is referred to [1], [11] and [12] for a more detailed report on kinetic mixing.

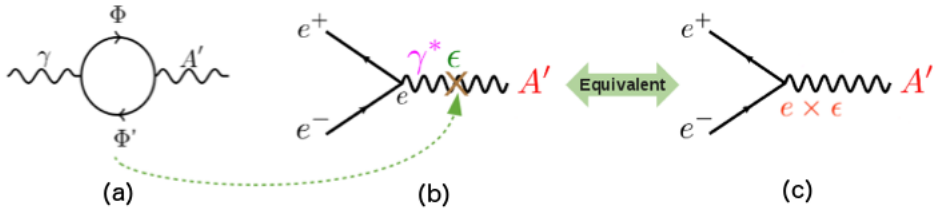


Figure 1.2: Diagrammatic representation of kinetic mixing showing the interaction of massive fields Φ and the subsequent coupling of the A' to electric charge $\epsilon$.e. Figure a) represents the kinetic mixing where a A' mixes with a standard model photon and is represented as X in b). b) represnts the process A'$\rightarrow e^+e^-$ and c) shows the detectable process as it would appear in the Standard Model sector.

The coupling to electric charge allows A' to decay to Standard Model lepton pairs which can be produced in either annihilation or decay. For the former process, two dark matter particles annihilate producing a pair of heavy photons (A') which may then produce lepton pairs, see Figure 1.3. The decay process is where a single A' is emitted from a dark matter particle which may then produce a standard model lepton pair. The final state of the dark particle is unknown within the Hidden Sector, see Figure 1.4 [4].

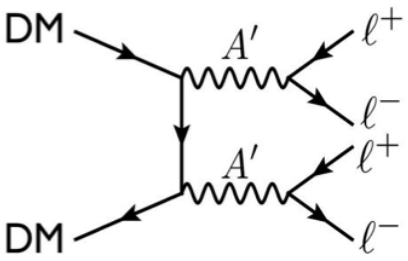


Figure 1.3: Diagram describes the process of A' from dark matter annihilation. Two massive dark matter particles annihilate producing a pair of A' which each may produce lepton pairs.

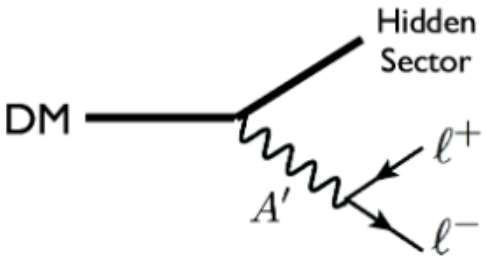


Figure 1.4: Diagram describes A' production from dark matter decay. An A' is produced in the decay that may then produce a lepton pair. The final state of the dark matter particle is unknown in the hidden sector

The type of leptons produced is dependant on the mass of A'. One of the ways that A' is thought to acquire its mass is through the Higgs mechanism and is predicted to be in the mass range $m_{A'} \lesssim$ GeV [13]. The mass of A' determines the branching ratio and hence the resulting Standard Model decay states, $e^+e^-, \mu^+\mu^-$, etc. Figure 1.5 illustrates the branching ratios for the different possible states that an A' could decay to over a range of $m_{A'}$. At $m_{A'} \leq 2m_\mu$ the majority of dark matter will annihilate to $e^+e^-$. When $m_{A'} \backsim 700\ MeV$ dark matter would predominately decay to pions, reducing the probability of $e^+e^-$ being produced in its annihilation. The production of Standard Model leptons would allow Dark Matter to be indirectly detected. [12].

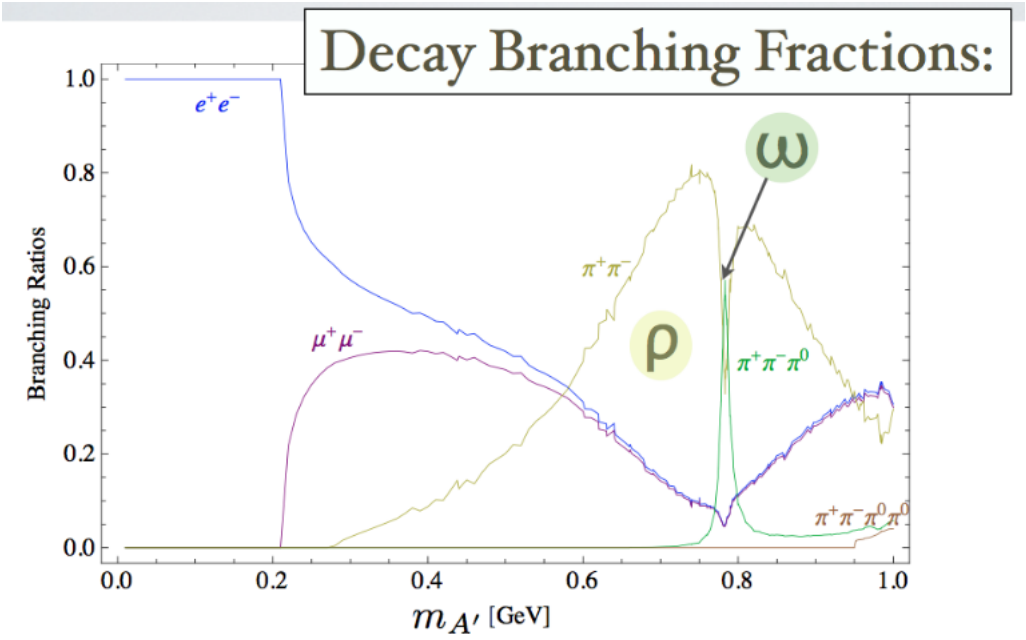


Figure 1.5: The branching ratio is dependant on the mass of the A' and describes the different possible states that A' can produce. The HPS experiment will be looking for leptonic rather than hadronic decays.

## 1.3 Observational Motivations

Galatic cosmic rays mostly consist of protons, electrons and ions. Primary sources of cosmic rays are particles accelerated by astrophysical sources and secondary sources are particles produced in the interaction with interstellar gas [14]. Positrons and

electrons are mainly produced from interactions of cosmic ray nuclei and interstellar gas as a secondary production process. One way of investigating the primary production is by looking at the Positron Fraction, where the positron fraction is the ratio,

$$\frac{\phi(e^+)}{\phi(e^+) + \phi(e^-)} \tag{1.2}$$

and $\phi$ is the positron and electron flux. From mathematical models, if secondary production dominates the positron fraction then the fraction is expected to fall off smoothly with increasing energy. However, recent observations from multiple experiments have contradicted this and the positron fraction is flatter than predicted [2].

The Payload for Antimatter Exploration and Light-nuclei Astrophysics (PAMELA) is a satellite-borne experiment designed to study charged particles in cosmic radiation, predominately studying antiparticles. Using a permanent magnet spectrometer with a silicon tracking system and a variety of other particle detectors, electrons and positrons can be distinguished in the impinging cosmic rays. The results of PAMELA have shown that the positron fraction increases significantly at energies above 10 GeV compared to predictions. Figure 1.6 clearly shows a sharp upturn in the positron fraction from 10 - 100 GeV [15].

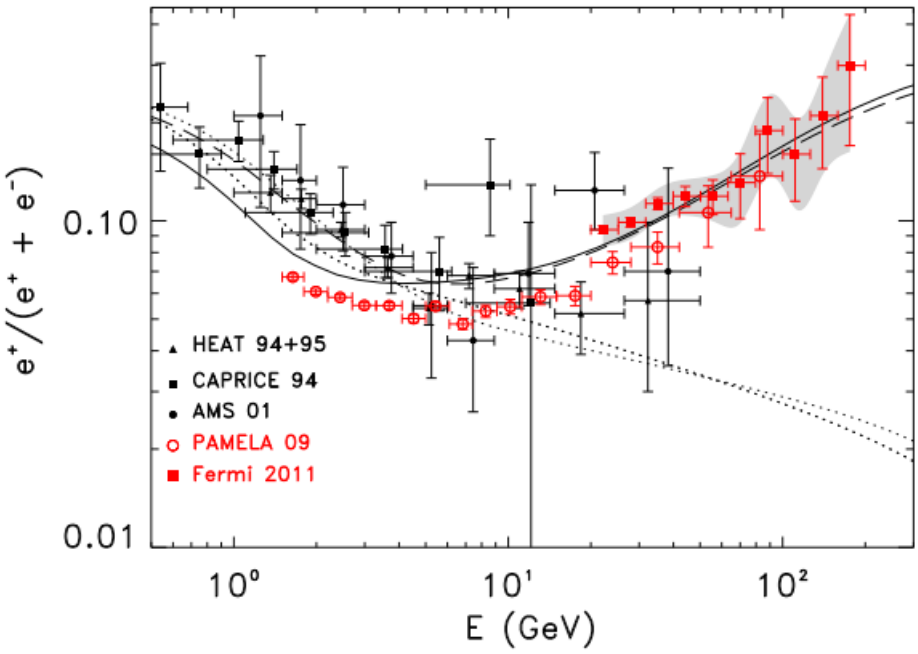


Figure 1.6: PAMELA results presented with the results from Fermi, AMS, CAPRICE and HEAT experiments showing an increase in the positron fraction compared to mathematical predictions. The predictions are represented as the dashed lines. The grey shaded area around the Fermi results represents the combination of both the statistical error and the systematic error, as the error bars represent the statistical error only.

Similarly The Advanced Thin Ionization Calorimeter (ATIC) measured an excess in the electron flux above 650 GeV. ATIC is a balloon borne detector consisting of a fully active bismuth germanate (BGO) calorimeter, a silicon matrix and scintillator hodoscopes. ATIC results, see Figure 1.7, show that below 100 GeV ATIC agrees with previous experimental observations and calculations and again at energies around 800 GeV. However between these two energies the ATIC spectrum peaks at about 650 GeV showing a clear excess in electron flux above values expected from GALPROP calculations [16]. GALPROP is a numerical code for calculating the propagation of relativistic charged particles and the diffuse emissions produced during their propagation.

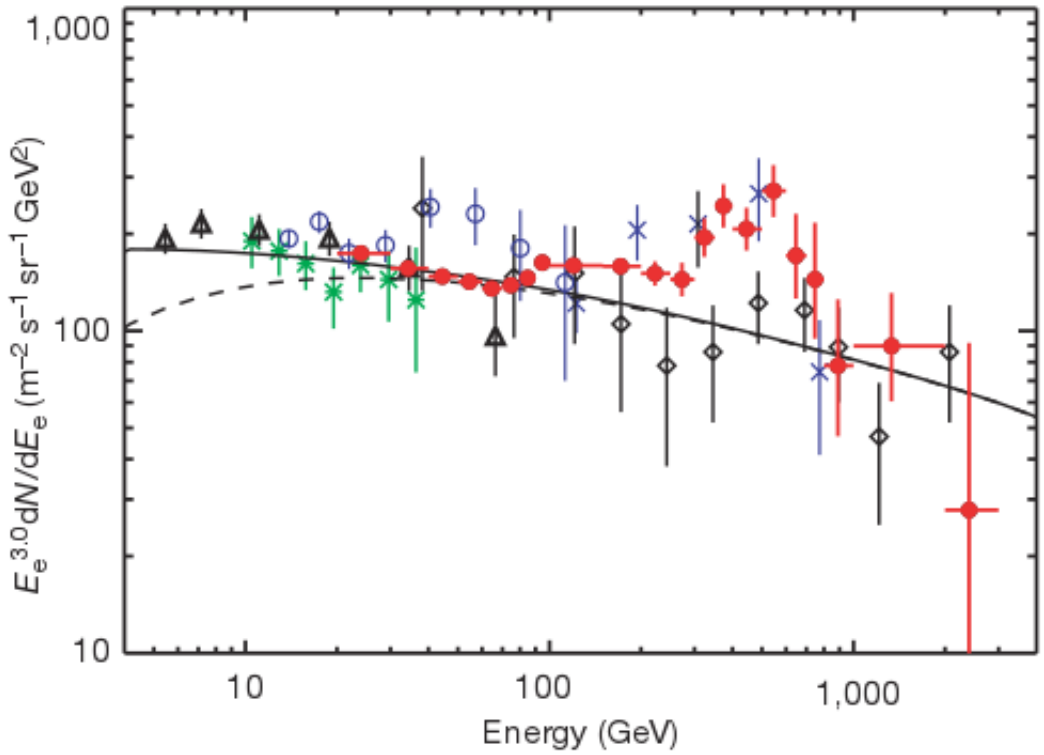


Figure 1.7: The electron differential spectrum (scaled by $E^3$) displaying the results from ATIC (red circles) compared with the results from other experiments, including the Alpha Magnetic Spectrometer AMS (green stars), HEAT (black triangles), BETS (blue circles), PPB-BETS (blue crosses) and emulsion chambers (black diamonds) in comparison to mathematical models (black lines)

Additionally, the Wilkinson Microwave Anisotropy Probe (WMAP), a spacecraft detector, has observed an excess in microwave emission from the galactic centre [17]. The microwave emission could be explained by the synchrotron radiation produced from electron and positron excess measured by PAMELA, ATIC and the other experiments.

These results collectively provide evidence that the galaxy has an excess of electrons and positrons. For each of these findings, there may exist a standard model astrophysical process that could explain these results [11]. However no unified standard model explanation has been proven and the lepton pairs produced in dark matter annihilation and decay could also account for this excess. Further support-

ing this is the proton anti-proton flux measured by PAMELA [2]. There was no excess observed when comparing measured data to predictions, see Figure 1.8. This places a constraint on the mass of the A', which agrees well with the theoretical prediction, $m_{A'} \lesssim$ GeV, meaning that it is kinematically impossible for the A' to decay to protons and anti-protons [4].

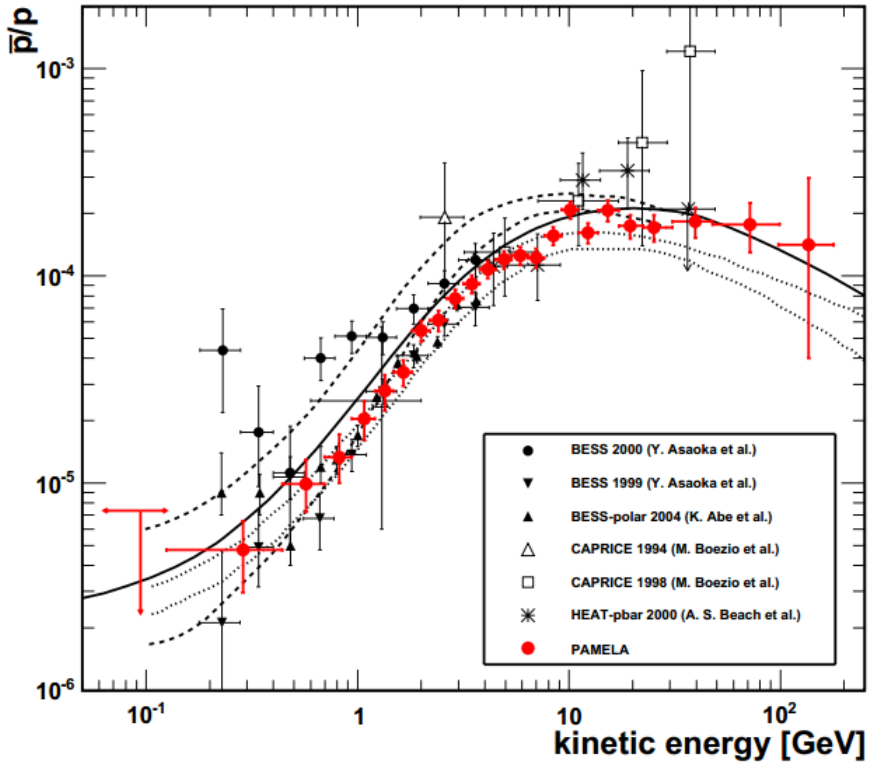


Figure 1.8: Proton fraction measured in PAMELA and several other experiments have matched predictions, represented by dotted lines.

## 1.4 A' Measurement

Although some constraints on the mass of the A' are forthcoming from astrophysical data, the cosmic ray excess does not point to a specific parameter space, therefore multiple experiments are looking for A' in different ranges of $\epsilon$ and $m_{A'}$. Figure 1.9 shows the different areas of parameter space that is being experimentally studied. The shaded areas are past experiments which have not observed A' providing constraints for future experiments. Future and proposed experiment ranges are illustrated by solid lines [19]. Recent results for Phenix and APEX are given in [18]

and [3], respectively.

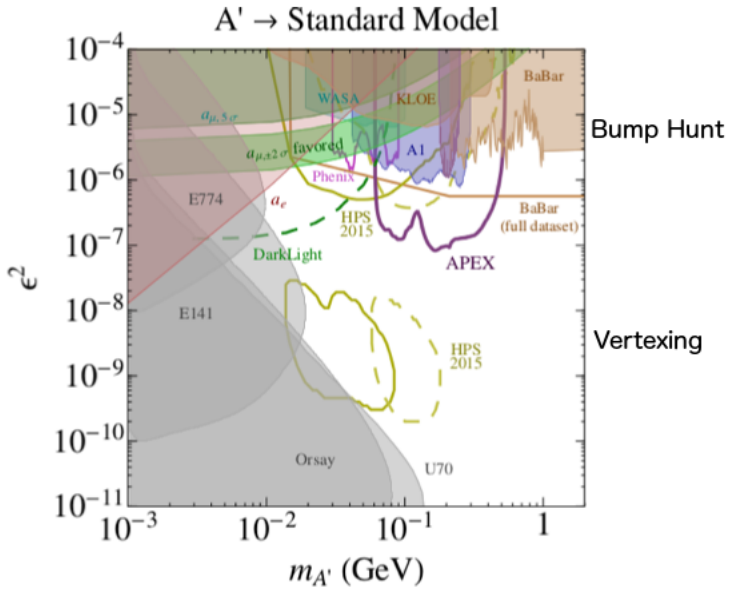


Figure 1.9: The existing constraints of A'. The shaded areas represent areas of parameter space that have either been tested or excluded in cosmic data. These areas have not found evidence of the existence of A'. The solid colour lines represent future experiments including the HPS Experiment which plans to cover two different areas of parameter space using two different measurement techniques. The solid HPS lines represent areas that will be tested during experimental runs in 2014 and the dotted lines represent experimental runs in 2015.

The Heavy Photon Search (HPS) experiment will measure two areas of parameter space using two different measuring techniques: a bump hunt and vertexing which will be described below. An electron beam will impinge on a tungsten target intended to produce an A' by a process analogous to ordinary photon bremsstrahlung. This production process is illustrated in Figure 1.10 where an incoming electron scatters from an atomic nucleus Z [20].

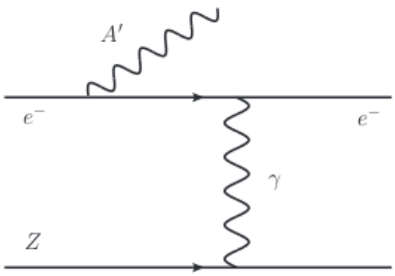


Figure 1.10: A' production from an electron beam impinging on a fixed target. The process is analogous to normal bremsstrahlung but with some differences in rate and kinematics

However, there are important differences in the rate and kinematics between A' production and an ordinary photon production. The total production rate of A' is much lower than that of ordinary photon production and is characterised by $\alpha^3\epsilon^2/m_{A'}$. A' production is therefore suppressed relative to photon bremsstrahlung by $\backsim \epsilon^2 m_e^2/m_{A'}^2$. A' is expected to be emitted predominately at small angles meaning that it will carry the majority of the beam energy ($E_{A'}/E_{beam} \approx 1$). Unfortunately, ordinary photon production may also dominate at small angles mimicking the A' signal. However the mean dacay length, $l_o$ of A' is predicted to be much longer than that of ordinary bremsstrahlung which may help distinguish between the A' and $\gamma$ production. The lifetime of A' can be determined using Equation 1.3 [12].

$$l_0 \equiv \gamma c\tau \backsim \frac{0.8cm}{N_{eff}} \left(\frac{E_0}{10GeV}\right) \left(\frac{10^{-4}}{\epsilon}\right)^2 \left(\frac{100MeV}{m_{A'}^2}\right)^2 \tag{1.3}$$

where $E_0$ is the beam energy and $N_{eff}$ is the number of final states that A' can decay to. $E_0$ and $N_{eff}$ limit the parameter space that HPS can cover, as there is a maximum beam energy that can be produced and the detector set up is designed to measure only $e^+e^-$ pairs. The ranges of $\epsilon$ and $m_{A'}$ that will be covered by the HPS experiment corresponds to a long lifetime due to a low coupling strength $\epsilon$. The long lifetime could result in A' travelling as much as tens of centimetres before decaying. For ordinary bremsstrahlung the lifetime is short and the production will decay to $e^+e^-$ pairs quickly and near the target.

QED processes will dominate the background signal making it difficult to determine if an A' was produced. The background rates are irreducible and are a

combination of two processes: radiative (Figure 1.11**(a)**) and Bethe-Heitler (Figure 1.11**(b)**). The radiative trident events are identical to A' signal events. However, information about the A' cross-section in relation to the radiative background rate can be obtained using Equation 1.4:

$$\frac{d\sigma(e^-Z \to e^-Z(A' \to l^+l^-))}{d\sigma(e^-Z \to e^-Z(\gamma^* \to l^+l^-))} = \frac{3\pi\epsilon^2}{2N_{eff}\alpha}\frac{m_{A'}}{\delta m} \tag{1.4}$$

Where $\delta$m is the mass width investigated and $N_{eff}$ is the number of final states that are open for A' to decay to [4].

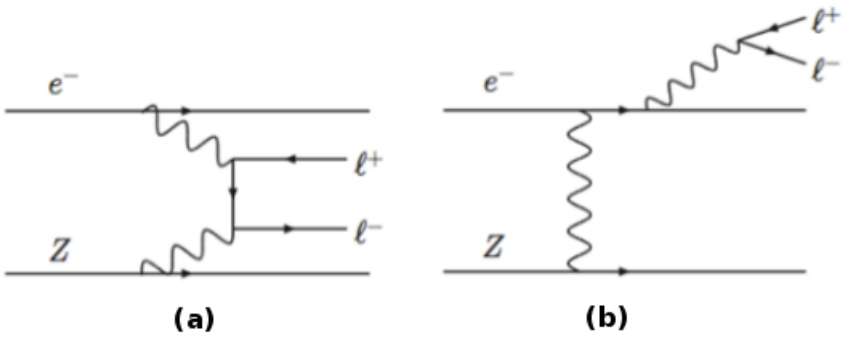


Figure 1.11: Feynman diagrams of the two QED processes that will dominate the background signal: Bethe-Heitler **(a)** and radiative **(b)**.

In comparison Bethe-Heitler has a much greater cross-section than both the A' signal and the radiative process however it can be reduced due to its differences in kinematics to the A' signal. An important difference is the energy, the A' is expected to carry the majority of the beam energy meaning that the recoiling electron scatters at a wide angle. For the Bethe-Heitler the recoiling electron is expected to carry the majority of the beam energy with the $e^+e^-$ produced by the bremsstrahlung photon having a much softer energy. This is represented in Figure 1.12, the Bethe-Heitler and radiative background shows a smooth continuous distribution in $m_{e^+e^-}$ and are generated close to the target. Conversely, the A' distribution is a peak at $m_{e^+e^-} = m_{A'}$ and an off-set from the target, since the A' is predicted to travel of the order of cm before decaying into $e^+e^-$ due to its low coupling strength. The features form the basis of the bump hunt and the vertexing techniques for identifying A',

see Figure 1.13 and 1.14. To help distinguish the background from A' signal good momentum and spatial resolution detectors are required [4] [12].

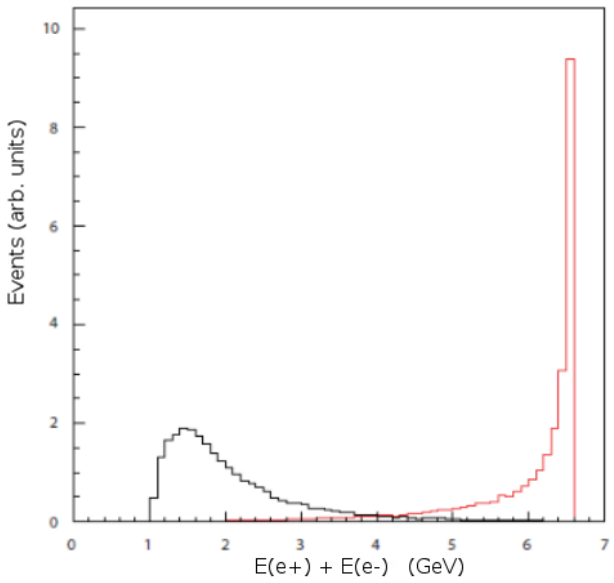


Figure 1.12: The sum of the electron and positron energy for both the Bethe-Heitler background (black) and A' signal events (red).

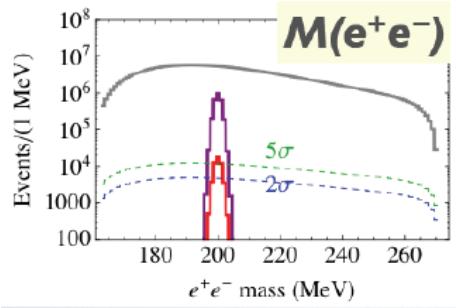


Figure 1.13: The bump hunt technique will look for the invariant mass A' in comparison to the invariant mass of the $e+e-$ QED background which is expected to have a wide distribution of values.

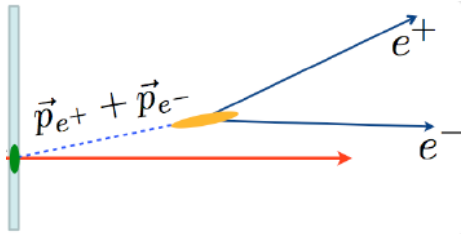


Figure 1.14: The vertexing measurement technique will exploit A' low coupling strength $\epsilon$, which predicted that A' will travel several cm before decaying to $e+e-$ pairs.

# Chapter 2

# HPS Experiment

The HPS experiment will take place in Hall B, Thomas Jefferson National Accelerator Facility (JLab), Virginia , USA. An electron beam produced in the Continuous Electron Beam Accelerator Facility (CEBAF) provides simultaneous beams to four experimental halls. Each hall contains different experimental set-ups researching a wide range of physics issues.

## 2.1 The Jefferson Lab Accelerator

The CEBAF is made up of two linear accelerators (linacs) and recirculating arcs, see Figure 2.1. Originally the CEBAF provided an electron beam to 3 different experimental halls: A, B and C, however on-going upgrades at the lab have increased the beam energy from 6 GeV to 12 GeV and an additional experimental hall, Hall D will be added. Electrons are produced by an electron gun made up of a laser, anode and photocathode. There are three lasers allowing three different electron beams with different characteristics to be produced dependant on what each experimental hall requires. The electrons are then accelerated in bunches along the linacs gaining energy in each loop. The two linacs are connected by a series of recirculating arcs. Before the arcs an initial magnet separates three different bunches dependant on their energies and sends them to corresponding dipole magnets. Each arc has its own set of dipole magnets with different bending strengths matched to the different electron energies. On leaving the arcs the bunches recombine to travel back through

the linacs. Once the required energy has been achieved a final magnet splits the electron bunches and sends them into the corresponding experimental halls [21].

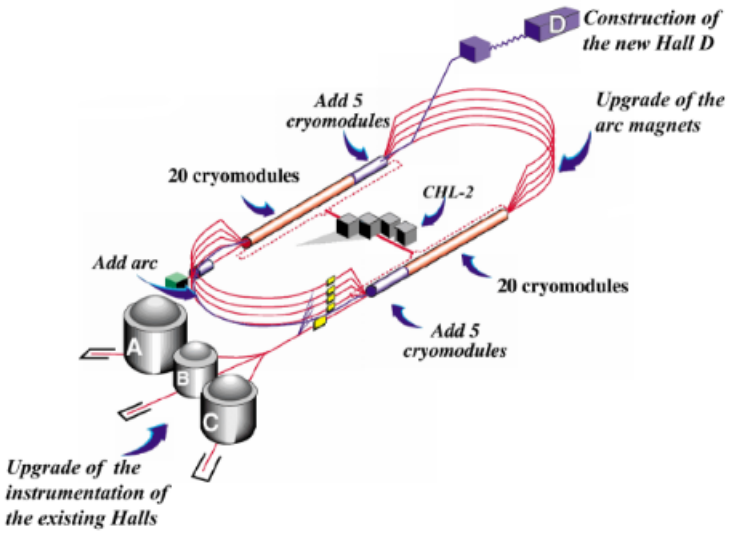


Figure 2.1: Schematic diagram of the upgraded Jefferson Lab showing the additional experimental Hall (D).

## 2.2 HPS Detector

The HPS Experiment will be located downstream from the CLAS12 experiment, both sharing Hall B [22]. The experiment will search for A', in the mass range from 20 MeV to 1000 MeV at three different electron beam energies. HPS will measure the invariant mass of A' decay products and the position of the decay vertex. The HPS detector package includes a Silicon Vertex Tracker (SVT) and an Electromagnetic Calorimeter (ECal). Figure 2.2 is an outline of the experimental set-up, which is based on a three magnet chicane: two dipole magnets (Frascati Magnets) and a pair spectrometer. The first Frascati Magnet focuses the beam and is located upstream from the SVT. The pair spectrometer will serve as the analysing magnet separating the $e^+e^-$ pairs and will be located above and below the SVT. The second Frascati Magnet, located downstream from the ECal, refocuses the beam which is transported to the beam-dump [4].

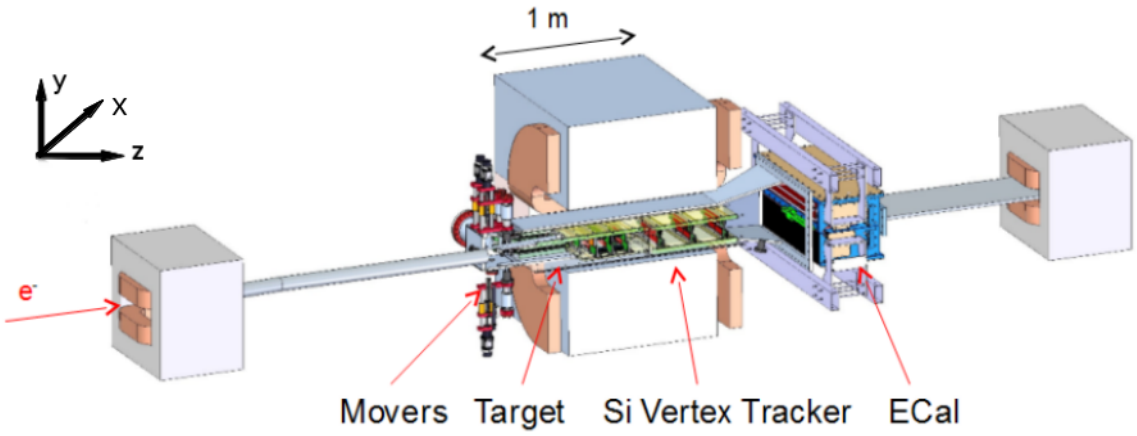


Figure 2.2: The HPS experimental set-up consisting of a Silicon Vertex Tracker (SVT), Electromagnetic Calorimeter (ECal) and a three magnet chicane. The outer dipole magnets are used for focusing and refocusing the beam. The pair spectrometer around the detector section separates $e^+e^-$.

The strength of the magnetic field will increase as the beam energy increases. The unscattered beam from the target will only be deflected by a small amount, whereas QED interactions with the target and potential A' decay products are expected to be deflected towards the planes of the SVT. The beam electrons will follow a curved path due to the magnetic forces, therefore there will be a gap in the ECal that is off-centre.

### 2.2.1 Electron Beam

The beam will be collimated to prevent the beam electrons from directly hitting the SVT. It will also be asymmetric to optimize vertexing performance and also to decrease the possibility of overheating the target. The design beam size is ($\sigma_X \sim 250$, $\sigma_Y \sim 50$) $\mu$m. The smaller beam width is required on Y to maintain a good vertex resolution for momentum measurements. This is less important in the X-direction therefore the beam width in X is larger to reduce the possibility of over heating the target [4].

### 2.2.2 SVT

The Silicon Vertex Tracker (SVT) will provide the kinematic information that is required to reconstruct an A' signal. The SVT is crucial for the vertex-based search: if the A' has a low coupling strength ($\epsilon$), it is expected to have a longer lifetime and therefore a displaced vertex. Information from the SVT is used to estimate the trajectory of the lepton pairs from which one can determine the vertex position. Momentum measurements are derived from the energy deposits in the ECal and vertexing from the SVT. The Momentum measurements can then be used to determine the mass of an A' and the SVT vertex position can be used to estimate the lifetime of an A'.

Figure 2.3 is a diagram depicting the SVT. The SVT has six layers, each layer having two closely spaced silicon planes with a gap allowing the beam to pass through. The first layer is 0.5 mm from the centre of the beam. The close proximity is required as A' is expected to be emitted at small angles relative to the beam line. This is to maximise the acceptance for low mass A'. However this proximity to the beam can add problems, for example sensors could be damaged or overloaded by the "wall of flame". The wall of flame is a combination of multiple Compton scattering from the beam and beam electrons which have radiated in the target, lost energy and scattered. The silicon planes are retractable from the beam allowing them to be moved during intervals of uncertain beam conditions [20].

The entire system is placed in a vacuum to limit primary beam interactions with air and will be temperature controlled. The silicon planes are actively cooled to mitigate the effects of radiation damage. The target will be located 10 cm upstream from the first layer of the SVT and is also encased within the vacuum [23].

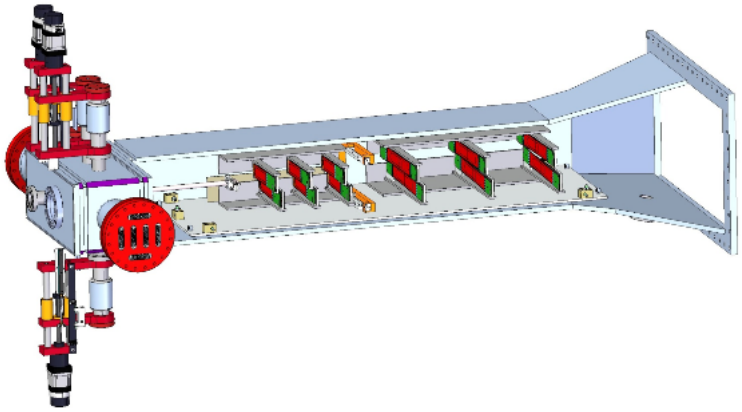

Figure 2.3: The Silicon Vertex Tracker consisting of 6 pairs of silicon planes, each plane separated to allow the unscattered electron beam to pass through. A tungsten target is placed 10cm upstream from the first plane as A' is expected to travel tens of cm at small couplings, $\epsilon$. The distance from the target to the front face of the ECal is $\sim$ 137 cm.

### 2.2.3 Target

The target material used in HPS is Tungsten. Tungsten is a favourable material as it has a high atomic number, Z, and a short radiation length, $X_o$. The high Z increases the probability of the electron beam interacting with the target (the scattering cross-section) and the short radiation length minimizes hadronic production. There will be two targets of identical size, 10 $mm^2$, but each having a different radiation length. The primary target is $0.00125X_o$ with the secondary target being $0.0025X_o$ which will be used when adjusting the beam current. The two targets will be located 10 cm upstream from the first silicon layer of the SVT and will be positioned inside the SVT vacuum. The two targets will be suspended from above, and have a support frame on three sides. The bottom edge of the target will not be supported to minimise the possibility of the beam tripping. The targets will be retractable from above allowing either thickness of target to be selected or to be completely removed from the beam line. A large beam spot size is required to minimise intense local heating that can lead to damage to the target. If one area of the target does experience damage the movable supports will allow the beam to impinge on other areas of the target.

### 2.2.4 ECal

The Electromagnetic calorimeter (ECal) will be located downstream from the SVT and will provide the trigger signal and identify the electrons and positrons. The ECal consists of 442 Lead Tungstate ($PbWO_4$) crystals arranged into two halves, top and bottom. Each half of the ECal has 5 rows each, four with 46 crystals and one with 37. There is a gap between the two layers providing space for a vacuum chamber. The gap is necessary to allow the beam and the wall of flame to pass through without overloading the ECal. The vacuum also eliminates beam gas secondaries and additional scattering. Figure 2.4 is a schematic diagram of the ECal set-up.

Each crystal is tapered with one small face with dimension 1.3 x 1.3 $cm^2$ and a larger face, 1.6 x 1.6 $cm^2$ and are each individually wrapped in VM200 polymer mirror film. Attached to the larger face is a Large Area Avalanche Photodiode (APD) (10 x 10 $mm^2$) that collects the scintillation light created in the $PbWO_4$ crystal. The APDs are connected to corresponding pre-amplifiers and electronics. On the smaller face an LED and LED holder is attached and is part of the Light Monitoring System (LMS). This system sends light pulses through the crystals to monitor radiation damage in the crystals and gain variations in the APDs. The small face is upstream and the large face is downstream. The pre-amplifiers are connected to motherboards (PCBs) that provide $\pm 5$ V and 400 V to the APDs.

Each half is supported by aluminium frames and encased in its own temperature controlled box set at $18^oC$. Maintaining a stable temperature is crucial as variations in temperature can change crystal light yield and vary APD gain [4].

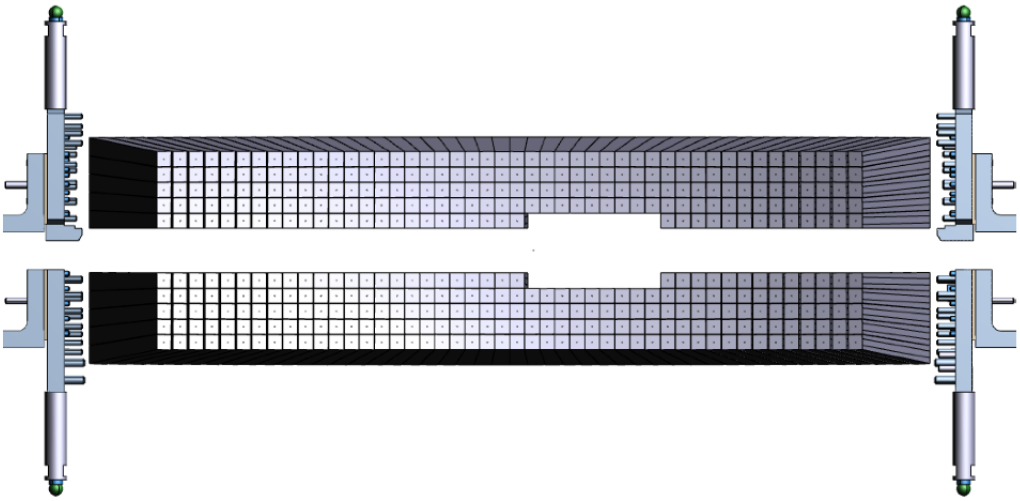

Figure 2.4: The ECal is split in two halves allowing the "wall of flame" to pass through and a vacuum chamber to fit in between. Each half consists of 221 $PbWO_4$ and is supported by aluminium frames.

### 2.2.5 Light Monitoring System

The Light Monitoring System (LMS) is required during the running of the experiment as the response of the ECal system can change in time. For example there can be variations in the gain of the APDs and loss in crystal transparency due to radiation damage [24]. To monitor these changes a LMS is attached on the front face of the ECal. The LMS will inject light pulses into each crystal and the light transmission will be measured. The light pulses will either be blue or red providing different information about the system. Blue light is sensitive to colour centres that form in the crystals due to radiation damage, whereas red light is less sensitive to colour centres, therefore monitoring the APDs and electronics more directly [25].

Bi-coloured LEDs (red/blue) will be mounted on the front of each $PbWO_4$ crystals using a plastic end-cap. The components of the system include 2 main controller boards, 8 driver boards, 4 connection boards and 442 LEDs. Using wires the LEDs are attached to a connection board providing communication via a USB to a computer that runs EPICS software. The software has multiple commands including the colour, frequency, pulse width and pulse amplitude of the LEDs. Each driver board hosts 56 independent LED pulser circuits and is attached to the LED connection

board. Figure 2.5 is a digram of the ECal, with each half in its thermal enclosure and separated by the vacuum box. The light monitoring electronics are visible on the front face [4].

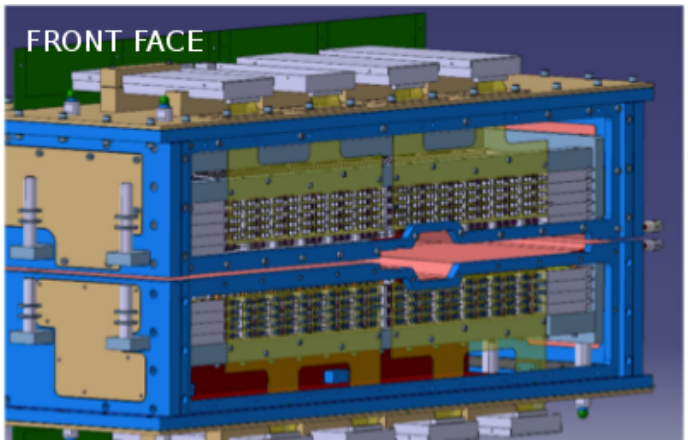


Figure 2.5: Schematic diagram of a full constructed ECal, the Light Monitorting System electronics shown on the front face.

### 2.2.6 ECal and Light Monitoring Components

#### Lead Tungstate Crystals

Lead tungstate ($PbWO_4$) crystals are commonly used in electromagnetic calorimetry due to their high density, fast decay time, short radiation length, adequate light yield and high tolerance to radiation [5]. $PbWO_4$ is an inorganic scintillator grown from 50% lead oxide (PbO) and 50% tungsten oxide ($WO_3$) [26]. The $PbWO_4$ crystal used in the HPS ECal was produced in the Bogoriditsk Technical Chemical Plant (BTCP) in Russia. Figure 2.6, is a picture of one of the ECal crystals.

Figure 2.6: Single $PbWO_4$ crystal used in the HPS ECal.

Scintillation light is produced in a crystal when an incoming charged particle excites an electron from the valence band to the conduction band, if the energy is sufficient. In the de-excitation process a photon is emitted within the crystal. Inorganic crystals are doped with impurities to increase the probability of a visible photon being emitted during the de-excitation process, see Figure 2.7. The scintillation photon can then convert to a $e^+e^-$ pair, the resulting pair can then further interact with the crystal via bremsstrahlung. The average length between two interactions in the crystal is quantified by the radation length $X_o$. This process is called an electromagnetic shower, See Figure 2.8, and is repeated approximately every $X_o$ until the photons fall below the energy required for pair production. An APD collects the light photons at the end of the crystal and a signal is recorded [27].

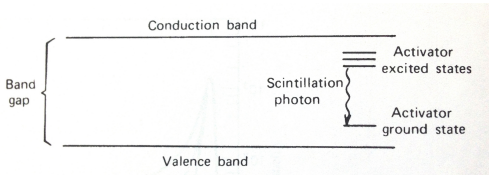


Figure 2.7: Illustration of the scintillation process in an inorganic crystal.

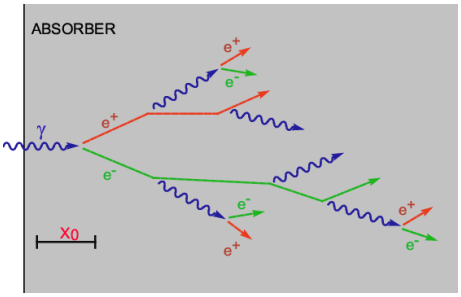


Figure 2.8: Electromagnetic shower.

$PbWO_4$ crystals have been greatly studied in recent years due to being used at leading experiments at CERN, for example CMS [26] and ALICE [28]. Table 2.1 displays some of $PbWO_4$ properties, including the the Moliere radius which describes the cylindrical area that contains 90% of the electromagnetic showers within the crystal. The peak scintillation emission for $PbWO_4$ is 420nm and the decay time can have several time constants; fast and slow components [24].

Table 2.1: Lead Tungstate ($PbWO_4$) crystal properties

| | |
|---|---|
| Density [g/cm$^3$] | 8.28 |
| Radiation Length, $X_o$ [cm] | 0.89 |
| Moliere radius [cm] | 2.2 |
| Peak Emission Wavelength, $\lambda$ [nm] | 420 |
| Decay Time [ns] | 5(73%), 14(23%), 110(4%) |

With electromagnetic calorimeters often being placed in highly radioactive environments it is important that the scintillation crystals are radiation hard. The most common type of radiation damage in inorganic crystals is due to the formation of colour centres [5]. When scintillation crystals are exposed to ionizing radiation, defects in the crystal may act as traps for electrons and holes. The defects become charged and have discrete energy levels allowing optical transitions to be induced. This can lead to scintillation light being absorbed as it travels through the crystal, which reduces the crystals transparency [26]. The colour centres can have absorption bands in a wide spectral region which are dependant on the crystal's chemical properties and impurities. Many studies have concluded that the scintillation mechanism itself is not damaged [24]. The colour centres can absorb the scintillation light that is produced or light from external sources that is shone through the crystal, therefore radiation damage reduces the overall light transmission of the crystal.

Colour centres are dependant on pre-existing defects in the crystals which can vary due to differences in growing techniques and also between different manufactures that produce the crystals. One study identifies six types of colour centres for $PbWO_4$ with absorption band ranges, 350-400, 420, 470, 520, 620 and 715 nm [26]. Specifically the absorption band at 360 nm is thought to be due an oxygen defect and

is often observed in different $PbWO_4$ crystals. Also, the absorption band at 420 nm can cause the crystal to turn yellowish in colour and could lead to the presence of holes trapped by lead ions [24].

There are two ways in which radiation damage in crystals can be recovered: spontaneous recovery or stimulated recovery. Either process will fully recover the damage however, on different time-scales. The relaxation of colour centres can be described by Equation 2.1 and 2.2;

$$n_i = n_0 exp\left(-w_T^i - \sum_j b_j I_j\right) t \tag{2.1}$$

$$w_T^i = A_i exp\left(\frac{-E_{TA}}{kT}\right) \tag{2.2}$$

where $n_0$ and $n_i$ represent the inital and current concentration of colour centres of type i. (Colour centre concentration is directly proportional to the number of defects in the crystal [26]). $w_T^i$, is the spontaneous relaxation probability and is a function of the thermo-activation energy of the colour centre, $E_{TA}$. $A_i$, T and $k$ are the normalisation constant, the temperature and the Boltzmann constant respectively. $b_j$ describes the interaction of the colour centres of type j, with a specific energy flux $I_j$ and t is the time period that the relaxation occurs [30]. Both i and j represent two different colour centre types. An example of two different types of colour centres are: shallow electron traps and Frenkel type defects (FTD), which cause deep electron centres. By leaving the crystal in a dark environment at room temperature for several weeks the damage will recover spontaneously via thermo-activation. This process is referred to as spontaneous relaxation and can be accelerated by thermally or optically annealing the crystals. Thermal annealing is possible due to $w_T^i$ dependence on temperature and is achieved by exposing the crystal to high temperatures. The recovery speed is temperature dependant, therefore increasing the temperature decreases the recovery time. A popular method of quickly annealing the crystal is by placing them in very high temperature ovens. Optical bleaching of the crystal involves injecting various wavelengths of light into the crystal and is reliant on high $b_j$ factors. Photons can ionize the colour centres if they have an energy equivalent to the energy between the ground state of the colour centre to a radiating excited

level [5].

For the HPS crystal thermal annealing would be impractical as removing the crystals from the ECal would be time consuming and could not be done during the experimental run. Spontaneous recovery occurs over too long a time period. Optical bleaching of the crystal is an attractive method as the LED light sources from the light monitoring system could be used for the dual purpose of both monitoring the radiation damage in the crystal as well as annealing the damage.

### Large Area Avalanche Photodiodes

Avalanche Photodiodes (APDs) are highly sensitive semi-conductor devices which convert visible light into current through the photoelectric effect. APDs are used in various experiments that require electromagnetic calorimeters, such as the CMS detector at CERN [25], PANDA [31] and the Forward Tagger Calorimeter (FT-Cal) [32], for the CLAS12 experiment at JLab. They are a solid state analogous to photomultipliers (PMTs) with similar performance but are superior in a number of ways. For example, they are insensitive to magnetic fields, have high quantum efficiency, a low power consumption and are small in size. The small size and insensitivity to magnetic fields particularly make them an ideal candidate for the HPS ECal. However there are a few limitations, such as high noise, low gain and susceptibility to radiation damage. Due to the low gain, and therefore a small output signal, pre-amplifiers are required [36].

Incident photons produce electron-hole pairs in the depletion region of the semi-conductor in an APD, provided that the photon energy is greater than the band gap energy. Applying a reverse voltage causes the electron-hole pairs to drift towards their respective anode and cathode at a speed dependent on the electric field strength. However, if the electric field is increased to a certain level, the charge carriers are more likely to collide with atoms in the crystal lattice. This resultant ionisation causes more electron-hole pairs to be created, some of which go on to cause further ionisation consequently giving a gain in the number of electrons. This process is refereed to as avalanche multiplication of photo-current [35], [34]. Figure 2.9 is an example schematic diagram of an APD.

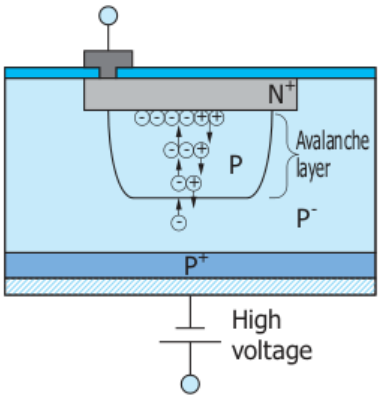


Figure 2.9: Schematic diagram of an APD.

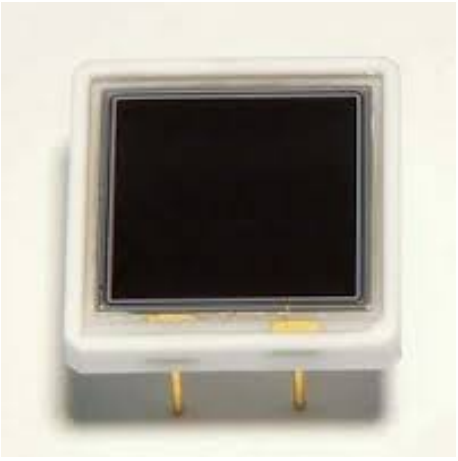

Figure 2.10: Large Area APD used in the HPS ECal. Model s8664-1010, Hamamatsu Photonics

The Large Area APDs that fit the requirements for the HPS ECal are the Hamamatsu Photonics s8664-1010 model, see Figure 2.10. They have a photosensitive area of 10x10mm$^2$ and are made of silicon encased in ceramic. Table 2.2 summaries some specifications that are provided by the manufacturer [36]. The quantum efficiency of the APD varies with wavelength (the ratio of the number of initally generated electron-hole pairs to the number of incident photons). A quantum efficiency curve was provided by Hamamatsu, see Figure 2.11, measured at 25$^o$C. The plot has two efficiency curves which are dependent on the model of APD, the top curve represents the quantum efficiency of the APD model used in the HPS Ecal. The peak emission wavelength for $PbWO_4$ is 420nm, giving the APD a quantum efficiency of $\simeq$ 70%.

Table 2.2: Large Area APD specifications provided by Hamamatsu

| APD model | S8664-1010 |
|---|---|
| Effective photosensitive area (mm$^2$) | 10 x 10 |
| Spectral response range (nm) | 320 to 1000 |
| Peak sensitivity wavelength (nm) | 600 |
| Quantum efficiency at $\lambda$ = 420nm | 70% |

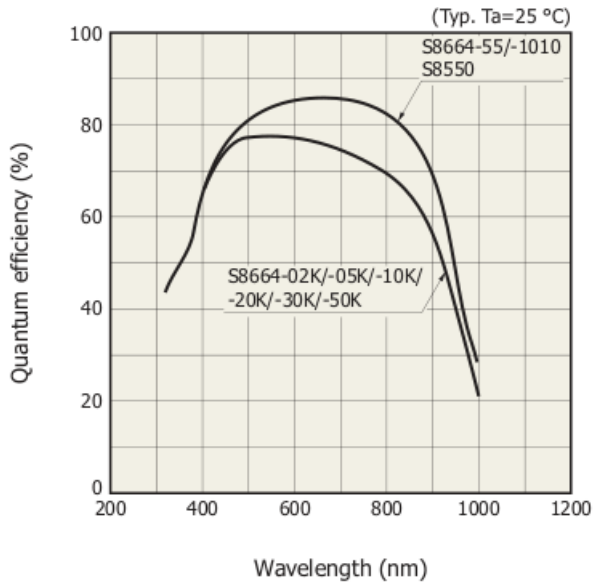


Figure 2.11: Quantum efficiency from data book provided by Hamamatsu (ECal APD shown by the top trend line)

### Light Emitting Diodes

Using LED light sources provides many advantages over regular light sources. They produce little heat as they do not emit infra-red wavelengths and have a very long lifetime. However, heat can be produced in the device itself during the conversion of electricity to light leading to decreased light, though this is an effect only becomes apparent after long hours of operation.

The LED model used in the Light Monitoring System is 5mm RAPID 56-0352, from Tru Opto, see Figure 2.13. The LEDs are two-lead semiconductor devices that produce light photons through the process of electroluminescence. The colour of light is dependant on the semiconductor material and the band gap energy. Bi-coloured LEDs are two single LEDs wired in parallel combined in one package, see Figure 2.12. There are two leads that share a common cathode, therefore only one colour can be switched on at one time. The LEDs have an operating temperature between -30 and +80$^o$C. The manufacturer provided specifications including the emitted wavelength measured at 25$^o$C, see Table 2.3. The blue setting has a typical wavelength of 470nm which is close to the peak emission wavelength of $PbWO_4$. LEDs are temperature dependant: an increase in temperature causes the emitted

wavelength to increase, but the intensity decreases. This effect is due to an increased resistance in the circuit, when there is a temperature increase the current in the circuit is reduced resulting in a lower intensity of light. The light monitoring system will be placed in the thermally controlled, enclosed box of the ECal and will be kept at a constant temperature of 18$^o$C [37].

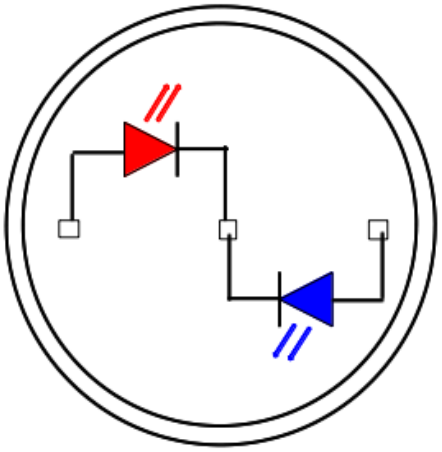

Figure 2.12: Bi-coloured LED wired inverse parallel sharing a common cathode, therefore a 3 pinned LED. The model used by the HPS LMS produces both blue and red light.

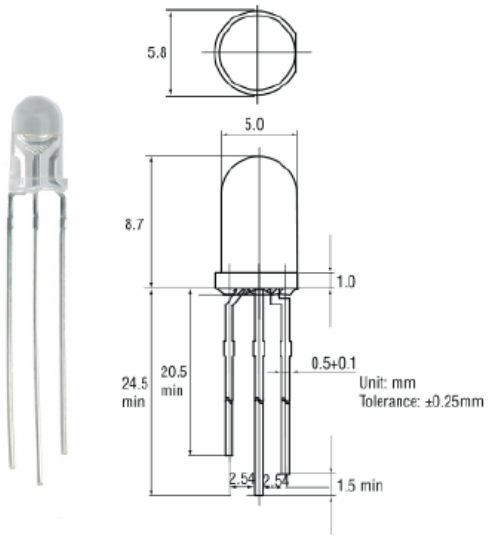


Figure 2.13: Schematic diagram of the Bi-Coloured LED.

Table 2.3: LED specifications provided by Tru Opto, measured at T=25$^o$C

| | Colour | Minimum | Typical | Maximum |
|---|---|---|---|---|
| Dominant Wavelength | Red | 620 nm | 625 nm | 630 nm |
| | Blue | 465 nm | 470 nm | 475 nm |

# Chapter 3

# ECal Component Tests

## 3.1 Radiation Damage and Recovery of Lead Tungstate Crystals

As described in Section 2.2.6, radiation damage due to the formation of colour centres is a well understood process. To quantify the specific damage that an HPS crystal would experience, irradiation tests were performed at the Strahlenzentrum at the University of Giessen, Germany. Additionally, optical bleaching is known to be a successful method of recovering the radiation damage. To determine if the blue LED from the light monitoring system would be efficient at recovering the damage, annealing tests were also performed. As a comparison, these tests were also carried out on a $PbWO_4$ crystal grown at another facility.

The HPS ECal crystal was produced at the Bogoroditsk Technical Chemical Plant (BTCP) in Russia. The crystal chosen as a comparison was produced at the Shanghai Institute of Ceramics, Chinese Academy of Sciences (SICCAS) and is a crystal that will be used in the Forward Tagger Calorimeter (FT-Cal), of CLAS12 which is an experiment also taking place in Hall B of JLab [32]. The two crystals differ in dimensions, both given in Table 3.1.

Table 3.1: The dimensions of the two $PbWO_4$ crystal tested. The HPS ECal crystal produced by BTCP and the CLAS12 FT-Cal crystal produced by SICCAS. The BTCP crystal is tapered to have one large face and one smaller face.

| | BTCP | SICCAS |
|---|---|---|
| Length [cm] | 16 | 20 |
| Face Dimensions [$cm^2$] | 1.3 & 1.6 | 1.5 |

### Quantifying and Measuring the Damage

The radiation hardness of a crystal can be quantified by calculating the radiation-induced absorption coefficient, *dk*:

$$dk = \frac{1}{L} ln \left( \frac{T_{bef}}{T_{irr}} \right) \tag{3.1}$$

Where $T_{bef}$ and $T_{irr}$ are the longitudinal light transmission before and after irradiation, respectively, and L is the length of the crystal. Crystals with greater damage due to radiation have a greater value of *dk*. Commonly for $PbWO_4$ crystals, *dk* is calculated at 420 nm as it is the peak emission wavelength [26], [30].

The longitudinal light transmission was measured using a Cary 4000 spectrophotometer at the Giessen facility. The spectrophotometer splits light from a lamp into multiple wavelengths using a diffraction grating. The diffraction grating is rotated allowing specific wavelengths through an exit slit, which leads to the crystal enclosure. A photo-diode measures the light at the opposite end from the light source [39]. The Giessen spectrophotometer has a custom enclosure that allows the measurement of light transmission through the longitudinal axis of a crystal. The light transmission is the fraction of light from the original light source that passes through the crystal and reaches the detector. The spectrophotometer is controlled by a computer that runs software displaying the measured transmission spectra. The spectrophotometer measures the transmission of the crystal for wavelengths 325 nm to 900 nm in 1 nm intervals. The laboratory was a dark room at room temperature, the only background light sources were a computer monitor and a red lamp. All measurements recorded by the spectrophotometer were saved as .csv files which allowed offline analysis using ROOT.

The facility also has an irradiation chamber located close to the spectrophotometer. The irradiation chamber consists of multiple $^{60}Co$ sources and multiple crystals can be irradiated at one time.

### 3.1.1 HPS ECal - BTCP Crystal

The longitudinal light transmission for one BTCP crystal was measured before the crystal was exposed to the $^{60}$Co sources. The crystal was then placed in the irradiation chamber for 15 minutes receiving a dose of 30 Gys. This dose rate equates to 1 month's worth of beam time expected for the CLAS12 experiment. This is therefore comparable with the HPS expected dose rate for 1 month as the two experiments share the same experimental hall. Once removed from the irradiation chamber the crystal was placed in a dark environment for 30 minutes. This is to allow the initial fast component of the spontaneous relaxation of the colour centres to occur, the relaxation process follows an exponential behaviour, see Equation 2.1 and 2.2. After the initial 30 minutes the crystal is expected to recover over a slower time-scale. The light transmission was then remeasured after this 30 minute period.

The BTCP crystal was then placed in a light-tight polystyrene container with a gap at one end for an LED. A Light Monitoring System bi-coloured LED was placed in the gap and the blue LED setting was switched to a continuous mode. The crystal was exposed to the blue light for short time intervals. Between these intervals the light transmission was retested using the spectrophotometer.

### 3.1.2 FT-Cal - SICCAS Crystal

The same measurements described for the BTCP crystal were applied to the SICCAS crystal. Additionally, light transmission measurements were taken during the initial fast spontaneous relaxation period. After 15 minutes in the irradiation enclosure the crystal was placed in the dark, light-tight crystal enclosure within the spectrophotometer. The spectrophotometer was set to automatically take light transmission measurements every 3 minutes for 30 minutes.

## 3.2 Radiation Damage and Recovery Results

### 3.2.1 HPS ECal - BTCP Crystal

The measured longitudinal light transmission before irradiation is represented by the black spectrum shown in Figure 3.1. The green spectrum represents the longitudinal light transmission measured after both the $^{60}$Co exposure and the initial fast spontaneous recovery. There is a clear decrease in light transmission seen across the visible spectrum, particularly between 400 nm and 600 nm. This demonstrates that colour centres are present in the crystal after irradiation. In Section 2.2.6 potential colour centres were identified with an absorption band range between 350 nm and 715 nm. The BTCP crystal appears to have all 5 colour centres with some centres causing greater damage than others [40].

The peak emission wavelength of $PbWO_4$ is 420 nm, however $PbWO_4$ has a broad luminescence emission band, thought to be a superposition of several luminescence bands. There are smaller emission wavelengths at 360 nm and 620 nm, therefore to better quantify the damage, *dk* was calculated at wavelengths 360 nm, 420 nm and 620 nm:

$\mathrm{dk}_{360nm} = 0.37 \pm 0.03\ \mathrm{m}^{-1}$, $\mathrm{dk}_{420nm} = 0.30 \pm 0.03\ \mathrm{m}^{-1}$, $\mathrm{dk}_{620nm} = 0.09 \pm 0.03\ \mathrm{m}^{-1}$

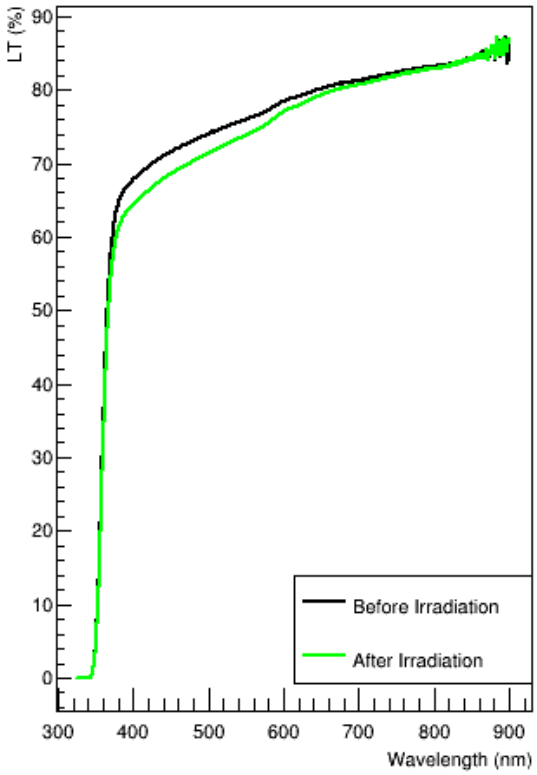


Figure 3.1: The longitudinal light transmission before (black) and after (green) irradiation damage due to $^{60}$Co exposure of the BTCP crystal. Clear decrease in light transmission over the visible spectrum due to the formation of colour centres, can be observed

After the previous measurement the crystal was exposed to the blue LED light. The left plot displayed in Figure 3.2 shows the before- and after-irradiation light transmissions previously measured and also the light transmission measured after 1, 3, 6, 9, 14, 25 and 36 minutes of the light exposure. The plot displayed on the right is the same data but shown over a smaller wavelength range. Each light exposure improves the light transmission through the crystal. This is evidently shown as each measured light transmission spectra increases in ascending order towards the before-irradiation light transmission spectrum, demonstrating the optical bleaching recovery effect.

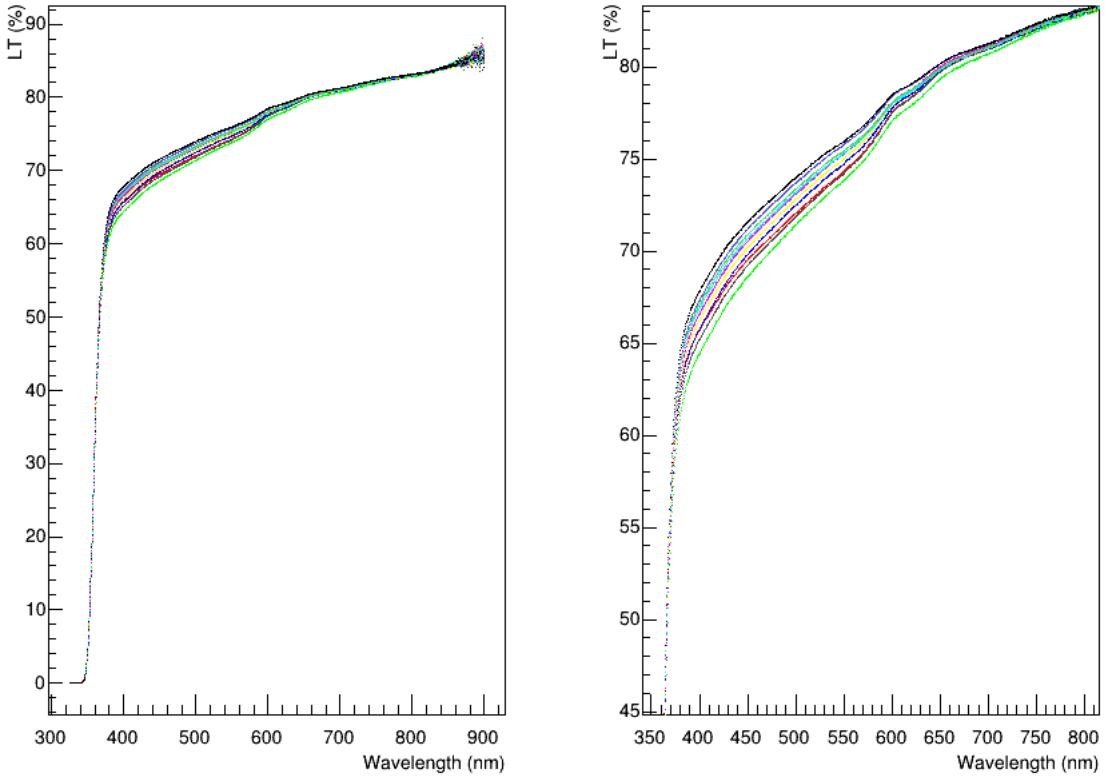


Figure 3.2: This plot includes the longitudinal light transmission spectra seen in Figure 3.1 and also the light transmission measured after 1, 3, 6, 9, 14, 25 and 35 minutes of blue LED light. There is visible improvement in the light transmission as each spectrum increases in ascending order towards the before-irradiated spectrum.

Specifically calculating $dk_{420nm}$ for each of the measurements and plotting them vs. time, displays the recovery effect more clearly, see Figure 3.3. There is a clear decrease in $dk_{420nm}$ as exposure time increases. After only 1 minute of light exposure there is a clear improvement in $dk$. After 35 minutes the crystal is almost fully annealed using the blue light.

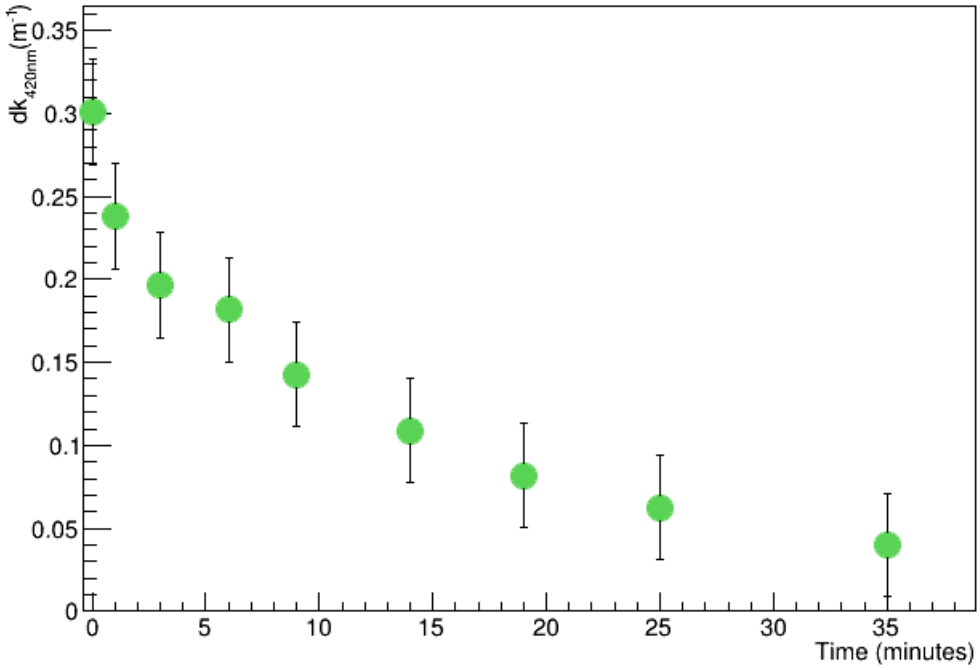


Figure 3.3: The radiation-induced absorption coefficient, $dk_{420nm}$ calculated for each measured light transmission spectrum vs. the blue LED light exposure time.

It is also interesting to calculate $dk$ for the full set of wavelengths measured. Figure 3.4 is a plot of the calculated $dk$, where the green trend represents $dk$ calculated using the pre-irradiation transmission and the transmission measured after the initial fast spontaneous relaxation. Some damage again is distinct between 350 nm and 700 nm with almost no damage seen at wavelengths greater than 800 nm. The blue trend represents dk calculated after 35 minutes of continuous LED light exposure. Some damage is still visible between 350 nm and 600 nm however the value of dk has greatly decreased.

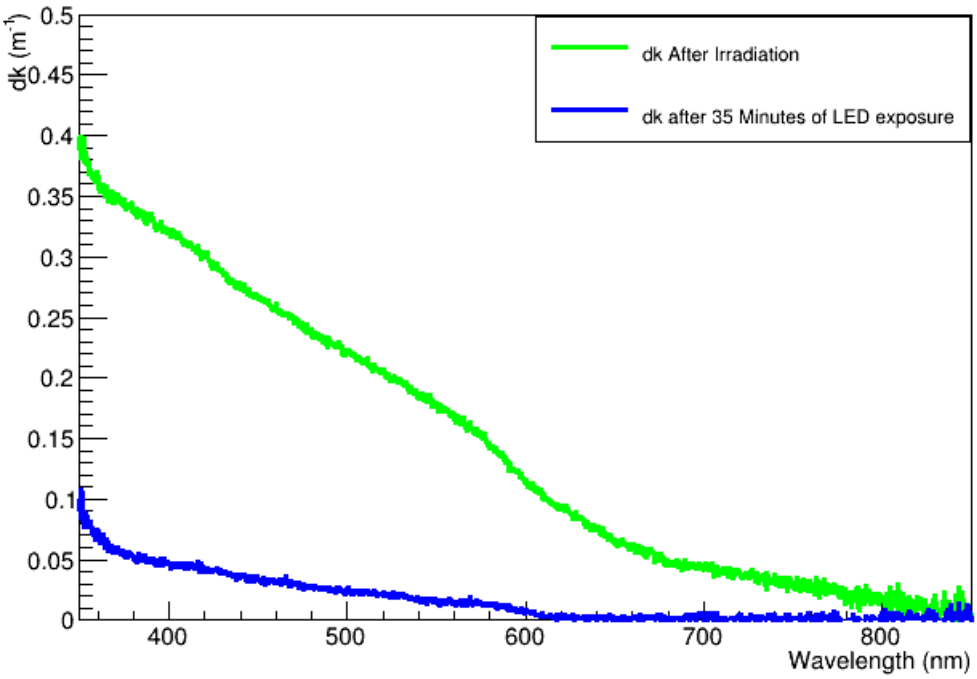


Figure 3.4: The radiation-induced absorption coefficient, $dk$ for the full wavelength range calculated after irradiation and again after 35 minutes of blue LED light exposure for the BTCP crystal.

### 3.2.2 FT-Cal - SICCAS crystal

The resulting light transmission spectra for the SICCAS crystal are shown in Figure 3.5, where the blue spectrum represents the light transmission before and the green spectrum represents the light transmission after irradiation and the initial spontaneous relaxation. There is again a noticeable reduction in the longitudinal light transmission over a wide range of wavelengths due to the formation of colour centres. The damage that is seen in the transmission for the SICCAS crystal is much greater than the damage experienced by the BTCP crystal (Figure 3.1). The calculated $dk$ values at 360 nm, 420 nm and 620 nm are:

$dk_{360nm} = 0.88 \pm 0.03\ \mathrm{m}^{-1}$, $dk_{420nm} = 1.13 \pm 0.03\ \mathrm{m}^{-1}$ and $dk_{620nm} = 0.443 \pm 0.03\ \mathrm{m}^{-1}$

In comparison to the BTCP crystal, $dk_{420nm}$ for the FT-Cal is almost 4 times greater. Therefore the SICCAS crystal is less resistant to radiation damage at that wavelength. Both crystals are $PbWO_4$, however they were produced by differ-

ent manufacturers and therefore in different conditions and environments. For the BTCP crystal $dk_{620nm}$ experienced greater damage than $dk_{420nm}$, for the SICCAS crystal this is not the case. The concentration of colour centres is dependant on the pre-existing defects in the crystal, which could be different for each manufacturer. This may explain the differences in $dk$ values.

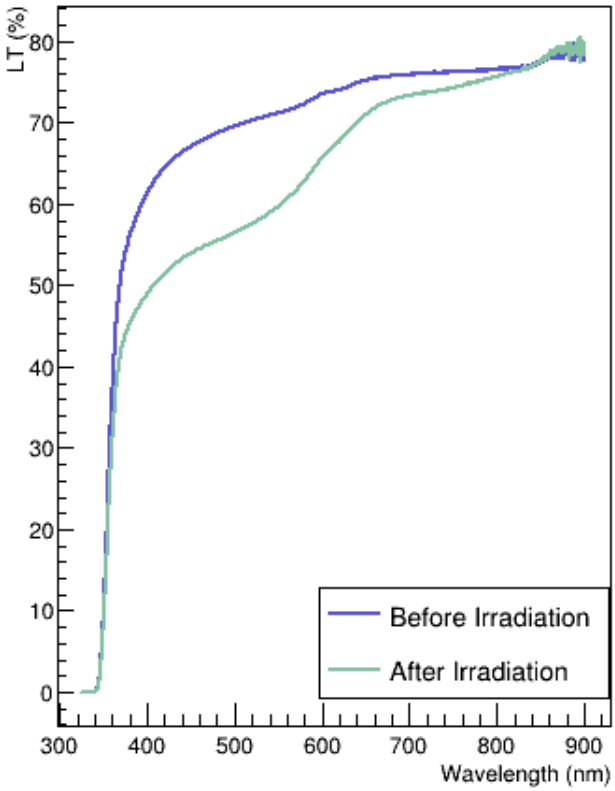


Figure 3.5: The longitudinal light transmission before (blue) and after (green) irradiation damage (and spontaneous recovery) due $^{60}$Co exposure of the SICCAS crystal. An evident decrease in light transmission is seen over the visible spectrum due to the formation of colour centres

The SICCAS crystal was exposed to the blue LED for smaller time intervals than the BTCP, with the light transmission measured after 30, 60, 100 and 130 seconds of LED light exposure. Figure 3.6 dispalys the spectra from the previous measurements and also the transmission remeasured after the blue light exposures. The plot on the right is the same data but over a smaller wavelength range to show the recovery

clearer. The initial recovery in the light transmission is much greater in comparison to the BTCP crystal as there is initially greater damage. This can be explained by the exponential behaviour of the relaxation process see Equation 2.1.

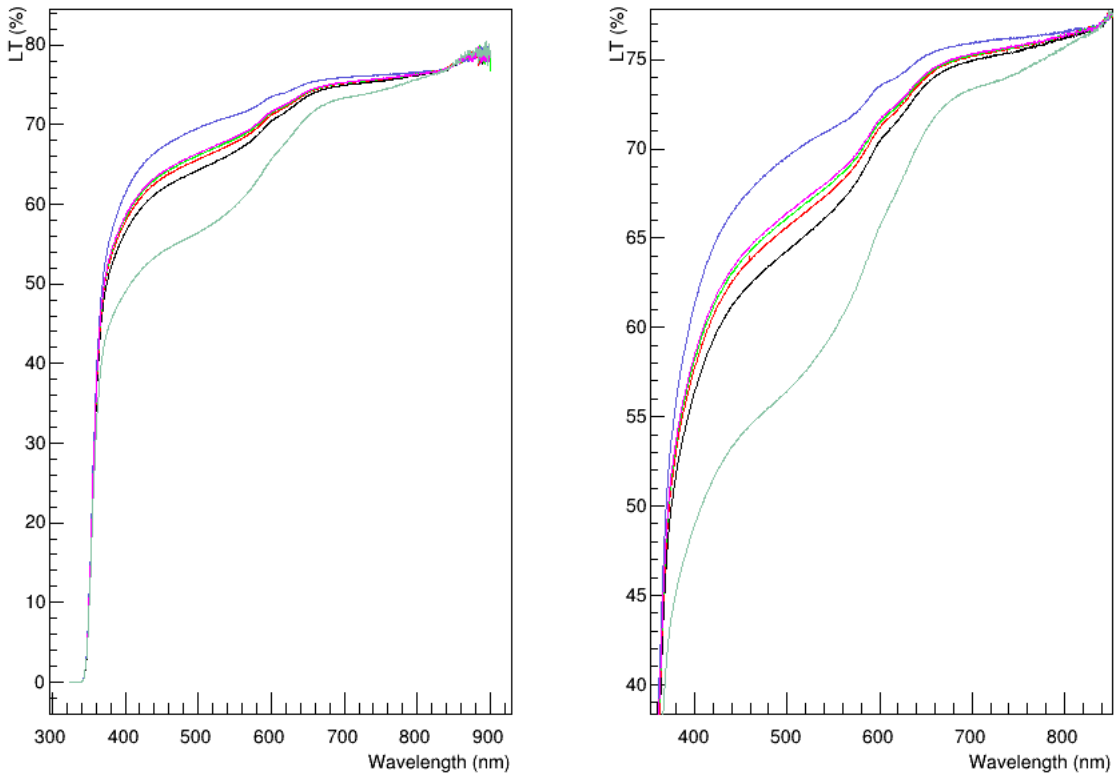


Figure 3.6: This plot includes the longitudinal light transmission spectra seen in Figure 3.5 and also the light transmission measured after 30, 60, 100 and 130 seconds of blue LED light. There is great improvement in the light transmission as each spectrum increases in ascending order towards the before-irradiated spectrum.

Figure 3.7 is a plot of the $dk_{420nm}$ for all light transmission measurements for the SICCAS crystal, where the x axis represents the measurement number. Measurement numbers 1-11 describe the measurements taken during the initial fast spontaneous relaxation, see left panel of Figure 3.8. Measurement numbers 12-15 represent the $dk_{420nm}$ values measured after the blue LED exposures, right panel of Figure 3.8. Measurement number 20 is $dk_{420nm}$ when the crystal is fully annealed; $dk_{420nm} = 0$ m$^{-1}$ which is expected for an undamaged crystal. There is a large decrease in $dk_{420nm}$ after the first LED exposure, following the expected exponential trend, clearly demonstrating the acceleration of crystal recovery using the technique

of optical bleaching.

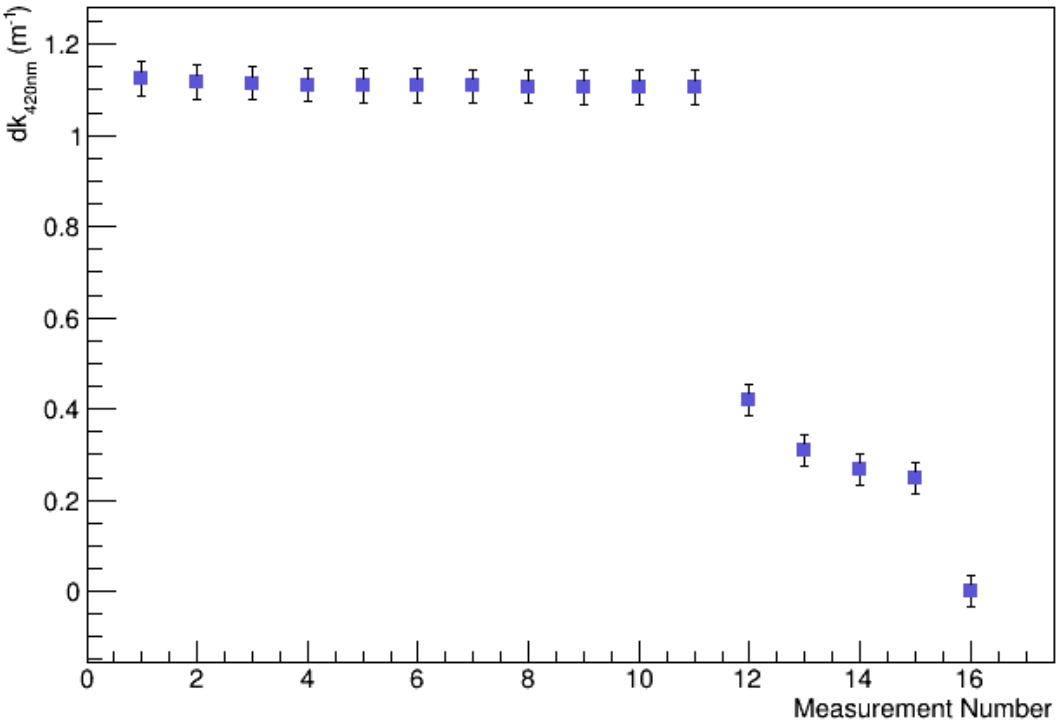


Figure 3.7: Calculated $dk_{420nm}$ for all light transmission measurements for the SIC-CAS crystal in the order of their measurement. Numbers 1-11 represent $dk_{420nm}$ measured during the spontaneous relaxation period and 12-15 represent $dk_{420nm}$ measured after blue LED light exposure. Number 16 is when the crystal is fully annealed. There is a great decrease in $dk_{420nm}$ after the initial exposure to the LED light.

The left plot in Figure 3.8 is the spontaneous relaxation $dk_{420nm}$ as function of time. The light transmission was automatically measured in 3 minute time intervals for 30 minutes while the crystal remained in the spectrophotometer crystal enclosure. The right plot in Figure 3.8 is $dk_{420nm}$ after 30, 60, 100 and 130 seconds of blue LED light. These plots both demonstrate that recovery of colour centres can occur though spontaneous relaxation or by stimulated recovery via optical bleaching. However the amount of spontaneous recovery that occurs within the 30 minutes is very small in comparison to stimilated recovery. For the crystal to recover spontaneously the

recovery process would occur over a much larger time scale than optical bleaching. Therefore optical bleaching would be a prefered method of recovery as it would anneal the crystal within a much smaller time period.

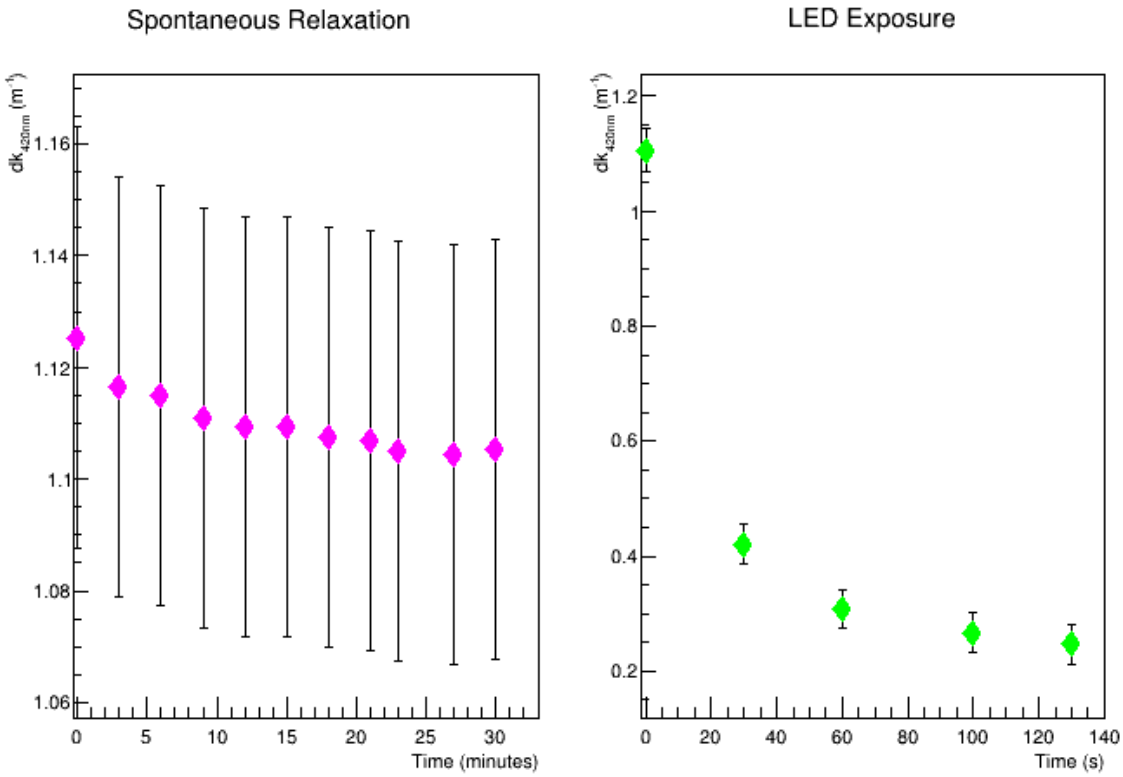


Figure 3.8: $dk_{420nm}$ measured during spontaneous relaxation (left) and the LED exposure (right), time-scaled. Both plots follow the expected exponential trend but on vastly different time scales, asserting that optical bleaching if efficient in accelerating the recovery of the colour centre. Considerable damage is visible, however a small improvement is seen after 30 minutes of spontaneous relaxation and vast improvement seen after 30 seconds of continuous blue LED light.

Finally, Figure 3.9 is a plot of the calculated $dk$ over the full range of measured wavelengths. The red line is $dk$ before initial spontaneous relaxation has occurred and the blue is $dk$ calculated after 30 minutes, which represents the recovery after spontaneous relaxation at room temperature. The green line is $dk$ after 30 seconds of continuous blue light exposure. In comparison to the BTCP crystal the damage experienced by the SICCAS crystal is much greater. There is clearly recovery in the

crystal within the first 30 minutes of being removed from the $^{60}$Co source due to spontaneous relaxation, however this is expected to slow as the behaviour of recovery follows an exponential trend. After only 30 seconds of blue LED recovery it is evident that optical bleaching is very efficient at recovering the radiation damage.

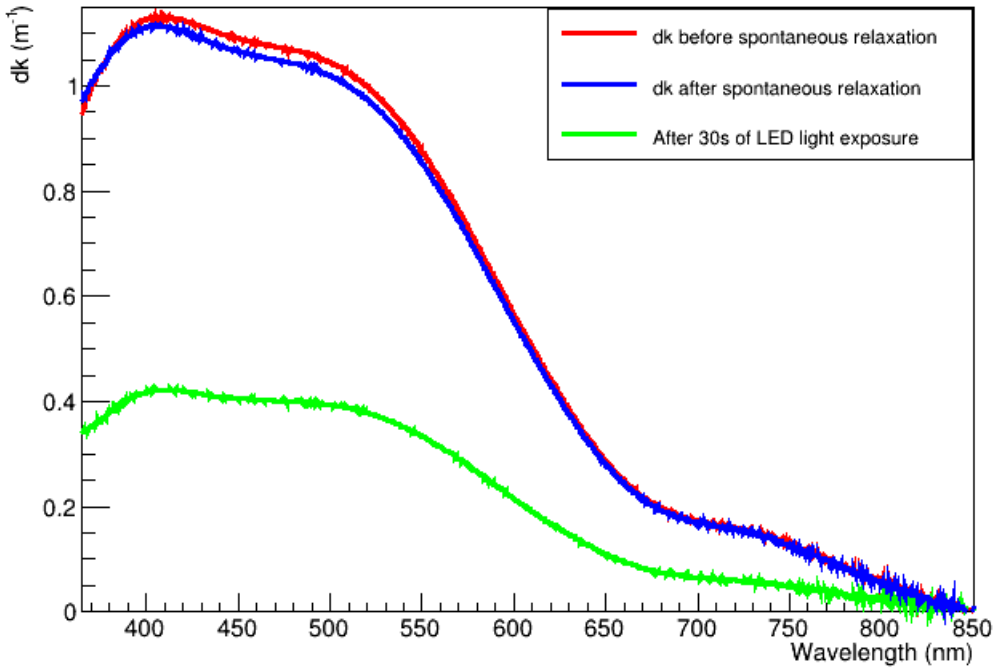


Figure 3.9: $dk_{420nm}$ for the full range of wavelengths measured. Considerable damage is visible however after 30 minutes of spontaneous relaxation there is a decrease in $dk_{420nm}$. The acceleration of the recovery using optical bleaching is demonstrated after only 30 seconds of blue LED exposure.

### Baseline Measurement and Crystal Positioning

Before and between multiple transmission measurements a baseline measurement was performed. The baseline is a reference measurement taken when no crystal is installed in the enclosure and no light is illuminated on the photodetector within the spectrophotometer. The left plot in Figure 3.10 is an example of a baseline measurement. The baseline was automatically subtracted from each transmission spectrum collected. The measurements were taken in room temperature conditions, however the temperature was not monitored. Temperature fluctuations can affect

the baseline measurement, therefore the baseline was measured initially when testing began and frequently between multiple measurements.

Another source of systematic error is the crystal positioning within the crystal enclosure. Small differences in the crystal position within the spectrophotometer can affect the measured light transmission. Therefore it was crucial that the crystal had the same orientation within for each measurement.

Even with the baseline subtractions and careful crystal positioning there was often still an observable shift between the two transmission spectra. The right plot in Figure 3.10 is an example of this behaviour. Both transmission spectra were measured before the crystal was exposed to the $^{60}$Co sources, therefore the spectra should be identical when superimposed. To fix this effect the data was normalised. This was achieved by calculating the average transmission between 800 nm and 900 nm for both spectra. This range was chosen as no radiation damage was observed in this wavelength region. The lower spectrum was then multiplied by the ratio of the two average transmissions. The ratio of the transmission between 800 nm - 900 nm for each spectrum ranged between 1.019 and 0.988 therefore the systematic error in the measurements is estimated to be 1-2%. Assigning an error of $\pm 1$ mm to the length of the crystal and averaging the transmission error to be $\pm 1.5\%$ allows an error on $dk$ to be calculated, on average the error was $\sim 0.03$ m$^{-1}$.

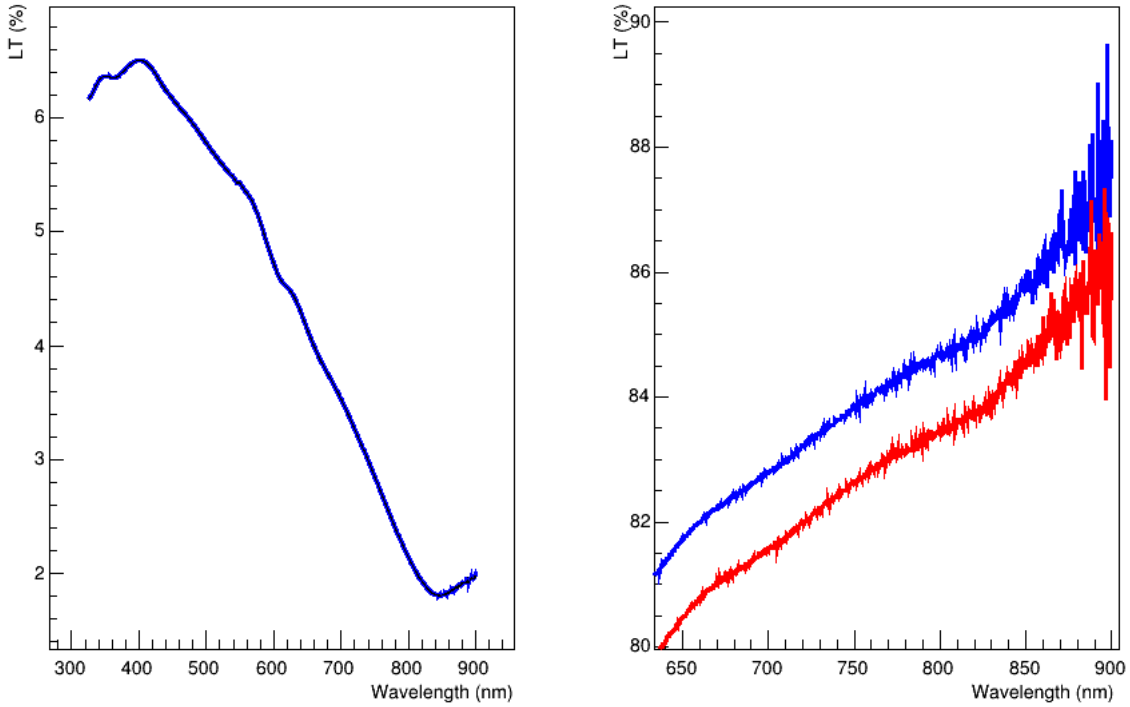


Figure 3.10: Baseline measurements were taken frequently between light transmission measurements and subtracted. On the left is an example baseline measurement. Each transmission was normalised as differences in crystal positioning caused shifts in the spectra, see right plot.

The spectrophotometer was not in a completely dark room, both computer monitor light and red lamps were present in the laboratory. Therefore between measurements the crystals were exposed to small amounts of background light. The light may have contributed to the crystal recovery, however the effect is expected to be small. This effect was minimised by storing irradiated crystals under a dark cloth and only removing the crystals to transfer to the spectrophotometer or to expose them to LED light.

### 3.2.3 Discussion

For both the BTCP crystal and the SICCAS crystal, there was a visible decrease in light transmission due to the formation of colour centres. The two crystals were grown by two different manufacturers and from these investigations the BTCP crystal appears to have a better radiation hardness.

It is evident that the blue LED from the LMS is sufficient at annealing both crystals and at a rate much quicker than spontaneous relaxation. The LEDs for the Light Monitoring System will be permanently attached to the front face of the ECal throughout the experimental run. It is expected that the Light Monitoring System will be switched on whenever the beam is off. The LEDs will be pulsed at high frequencies and not in a continuous mode. The radiation damage that occurs after 30 Gys is the expected dose of 1 month's beam time for the CLAS12 experiment and represents the extreme case. Throughout experimental run beams are often switched off, tripped or focused away from the experiment. During these times the Light Monitoring System can be used to anneal some of the damage in the crystal's. It is therefore unlikely that the crystals will experience the full damage observed in these tests. However, the gradual annealing and irradiation of the crystals results in an unstable light output. The light monitoring system is therefore required to manage the changes in crystal transparency as well as providing the light for optical bleaching.

## 3.3 Temperature Dependence of Scintillation Light Yield

The light yield of a scintillator is a measure of the number of photo-electrons produced per MeV of deposited energy [41]. In comparison to other scintillation crystals used in high energy physics detectors, $PbWO_4$ has a relativity low light yield [5]. At Giessen, a quick study was performed to quantify the light yield of a $PbWO_4$ crystal and determine its temperature dependence. This investigation was performed using SICCAS (FT-Cal) crystals as a BTCP (HPS ECal) crystal was not available at the time, but BTCP and SICCAS crystal are expected to have similar light yields.

### 3.3.1 Light Yield Measurement

The University of Giessen has a light yield testing-rig initially designed to perform light yield measurements for the PANDA experiment [31]. Figure 3.11 is a diagram representing the experimental set-up. A crystal was attached to a PMT and a $^{137}Cs$ source was placed at the other end. The PMT, crystal and source were located within a temperature controlled box that could be set to a range of temperatures. The PMT was connected to all the necessary electronics [41]. A series of measurements were taken at two different temperatures, $0^oC$ and $18^oC$, and using 4 different time gates, 100 ns, 200 ns, 500 ns and 1000 ns.

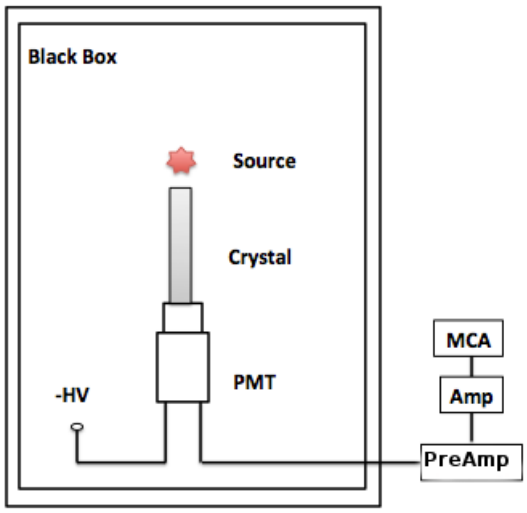


Figure 3.11: Schematic diagram of the light yield experimental set-up. A $PbWO_4$ crystal was placed in between a $^{137}$Cs source and a PMT all within a light tight temperature controlled box. The gamma-ray spectra were measured for two different temperatures and 4 different time gates [41].

The light yield (LY) for a chosen time gate (tg) can be calculated using Equation 3.2:

$$LY = \frac{[TEP(tg) - ped(tg)]}{[SEP(100ns) - ped(100ns)]}/E_\gamma \tag{3.2}$$

where TEP and SEP are the mean peak position of the total energy peak and the single electron peak, respectively. The single electron peak is a measurement of the electrons produced by internal conversion in the $^{137}$Cs atom. The total energy peak is prodimantly a measure of the $^{137}$Cs gamma rays interacting with the crystal via the photoelectric effect. Therefore the mean peak energy from this is equivalent to the incoming gamma ray energy, $E_\gamma$, which is 0.662 MeV for $^{137}$Cs. The SEP value measured for the 100 ns time gate can be used for the LY calculations at different time gates as the position of the SEP is not expected to change. The pedestal (ped) is a measurement of the non zero electronic charge measured in the PMT when no signal is present. The mean value of the pedestal is subtracted similarly to a background subtraction.

### 3.3.2 Light Yield Results

An example of one of the measured gamma-ray spectra is shown in Figure 3.12. The clear sharp peak on the left is the single photon electron peak and the total energy peak is on the right. If compared to a $^{137}$Cs gamma-ray spectrum measured using a NaI crystal, the total energy peak for $PbWO_4$ is much smaller and much wider [5].

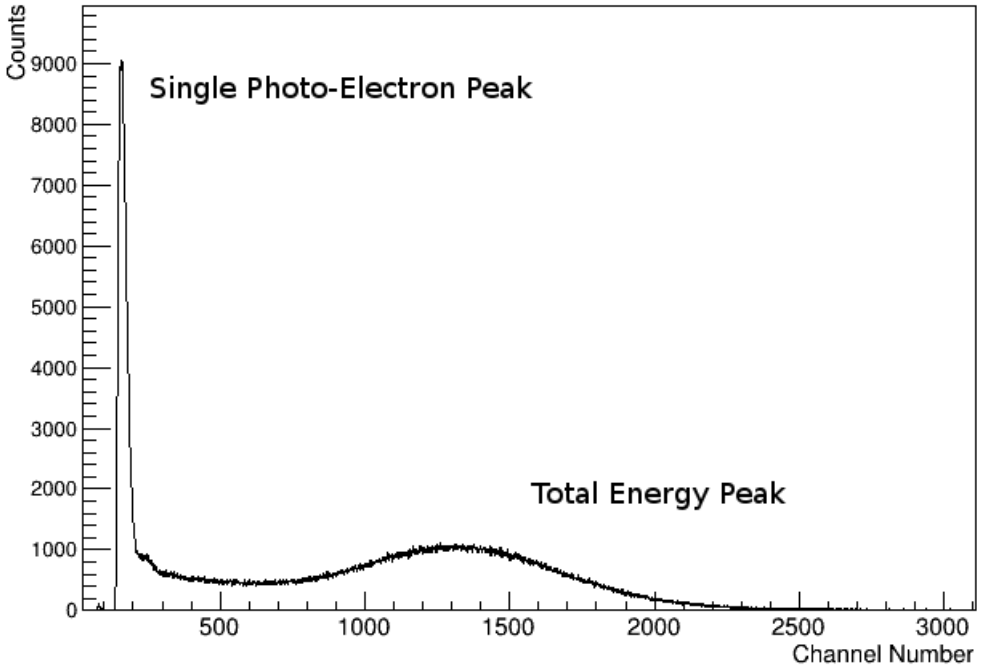


Figure 3.12: An example $^{137}$Cs gamma-ray spectrum measured at $0^oC$ with a time-gate of 100 ns.

For this investigation background measurements were not subtracted, therefore a Gaussian produced a bad fit to the peaks due to background contribution. To determine the mean peak position a combination of a Gaussian plus a parabola was fitted to each of the peaks to accommodate the background distributions, see Figures 3.13 and 3.14. From this the light yield was calculated using Equation 3.2.

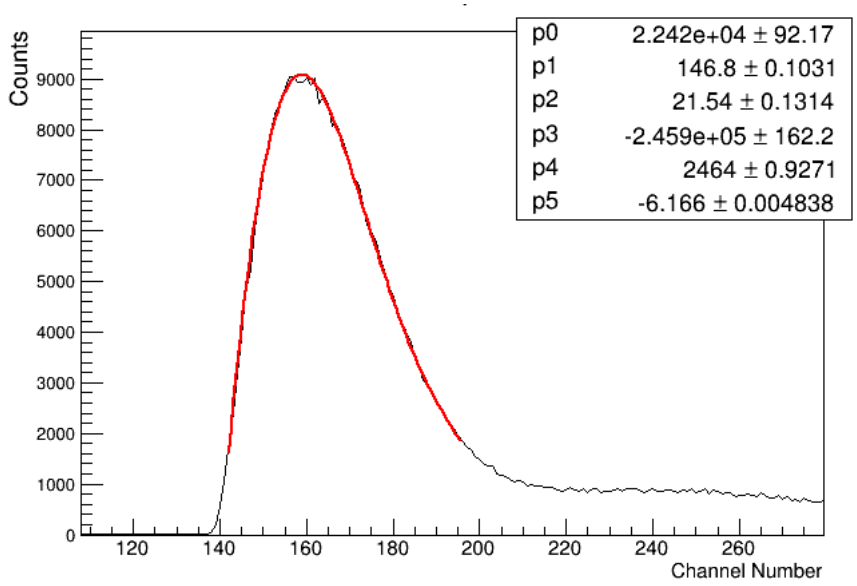


Figure 3.13: The single electron peak with a combination of a Gaussian plus a parabola fit to determine the mean peak position. The parabola is required to accommodate the background distributions that were not subtracted.

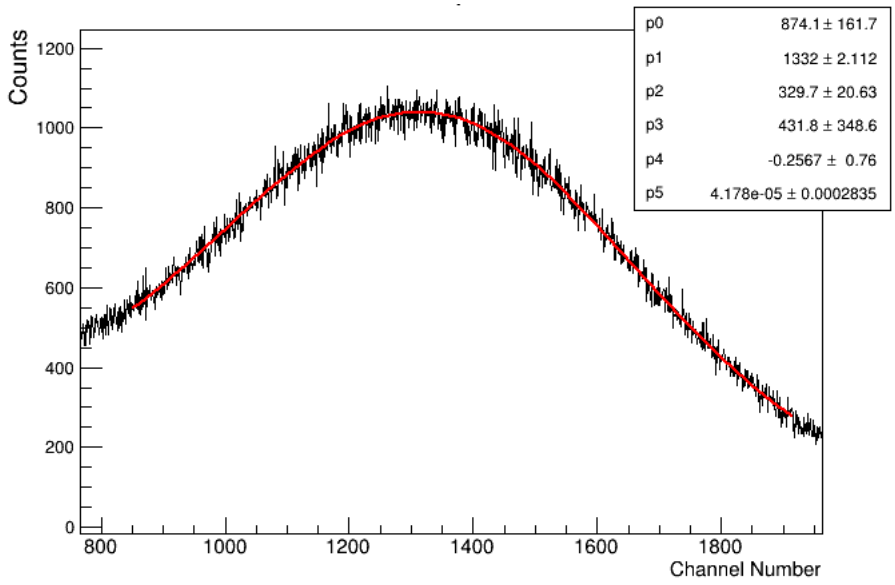


Figure 3.14: The total energy peak with a combination of a Gaussian plus a parabola fit to determine the mean peak position.

The light yield values for one crystal, calculated at two temperature settings and 4 time gates are shown in Figure 3.15. The x axis is scaled so that x=1 represents light yield measured at $0^o$C and x=2 represents light yield measured at $18^o$C. Each of

the different time-gates have an assigned symbol and are shifted by 0.1 increments to clearly show the light yield values. For each time-gate at a set temperature the light yield is roughly the same, within the error. However there is a significant difference in the light yield between the two temperatures. The light yield of $PbWO_4$ increases as the temperature decreases.

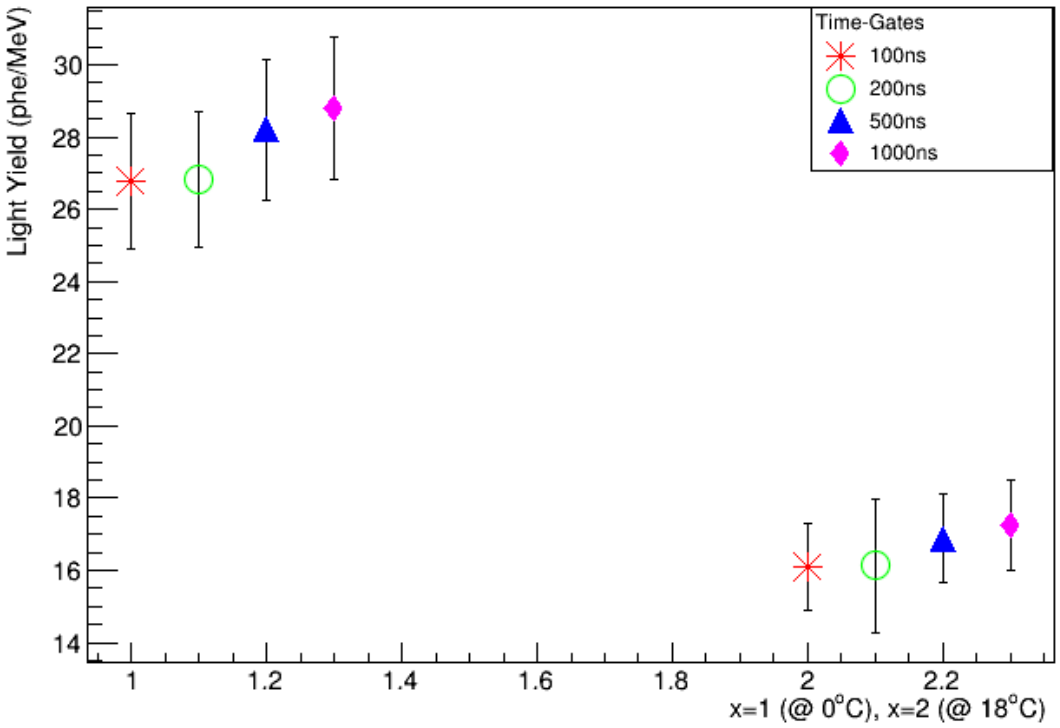


Figure 3.15: The calculated light yield for one crystal measured at $0^oC$ and $18^oC$ using 4 different time-gates. The x axis is scaled so that x=1 is equivalent to $0^oC$ and x=2 is $18^oC$ with an offset of 0.1 for each measurement. Within errors, the light yield is roughly the same for each time gate however there is a significant increase in light yield as the temperature is decreased.

The light yield was measured for 6 crystals: Figure 3.16 displays the calculated light yield for both temperatures with a time-gate of 100 ns. The x-axis is scaled similarly to Figure 3.15, however the points are shifted by 0.5 increments. The graph clearly shows that decreasing the temperature of the crystal increases the light yield. There is a spread in the light yield for each temperature, but mostly

within error. All crystals are consistent in trend to each other and follow a similar relative behaviour at both temperatures.

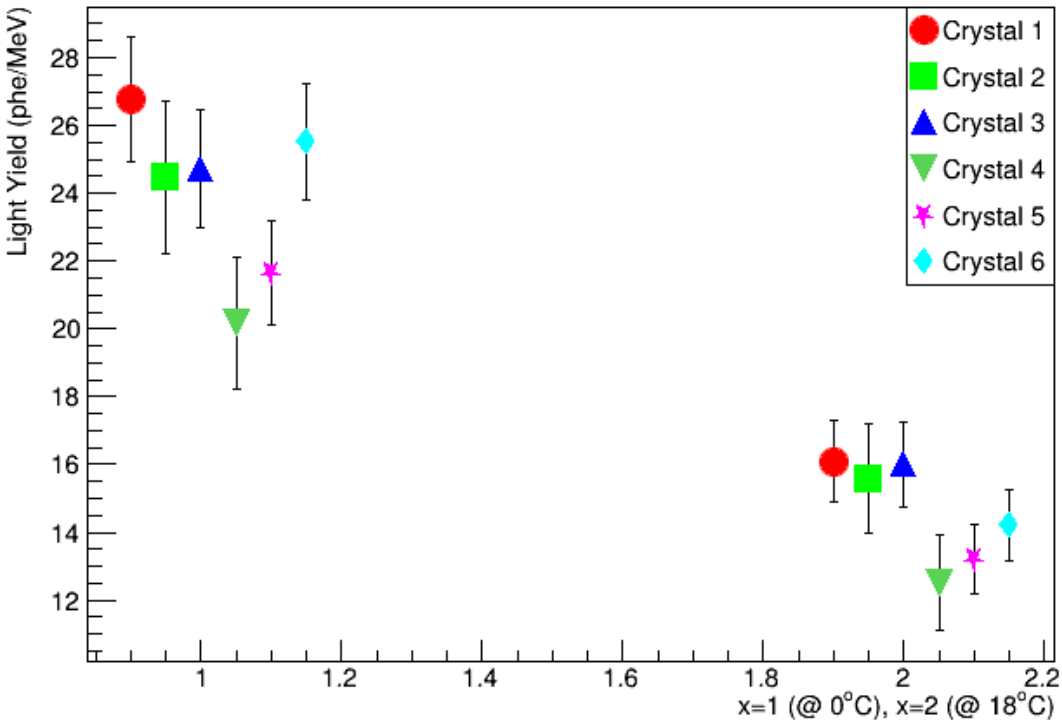


Figure 3.16: The light yield for 6 crystals measured at 0$^o$C and 18$^o$C with a time-gate of 100 ns.

Light Yield studies from the CMS technical design report [24], measure the light yield for a 23 cm long $PbWO_4$ crystal using a PMT. At a room temperature and a time-gate of 200 ns, the light yield was 'in excess of 10 phe/MeV' and the light yield gets worse by 2% per $^o$C. The PANDA technical design report suggests a slightly greater temperature coefficient of dLY/dT $\sim$ -3.0% per $^o$C [31]. For six crystal measured, the average light yields at a time-gate 100 ns are: 23.9 $\pm$ 0.8 at 0$^o$C and 14.6 $\pm$ 0.5 at 18$^o$C. Performing a quick percentage calculation, on average the light yield changes by $\sim$ -3.6% $\pm$ 0.5% when the temperature drops by 1$^o$C from 18$^o$C which is similar to what PANDA observe. To better estimate the light yield dependence and hence a more accurate temperature coefficient, the light would have to be measured at additional temperatures.

If the ECal temperature were to be decreased from its proposed run temperature of $18^oC$, the APDs would measure an increased light yield. However there are disadvantages that would need to be considered. For example, the radiation hardness of the crystal would decrease because the spontaneous relaxation rate would decrease due to the cooler temperature and the scintillation decay time would increase [32]. Due to these effects it was decided to keep the ECal running at $18^oC$ as the light yield is adequate for the requirements of the HPS experiment.

### Discussion of Uncertainties

The error on the light yield measurement was estimated using the Gaussian and parabola fits used to determine the mean peak channel number. Initially a Gaussian was loosely fitted to each peak to determine the mean. A parabola was then added to the Gaussian to incorporate the background distribution. This caused the mean peak to shift a number of channels. However, the parabola was an estimation of the background shape and still did not produce a perfect fit. The peak position is dependant on the fit function, so as an estimate of the error the difference between the mean peak channel measured using the initial Gaussian fit and the combination of the Gaussian + parabola fit was used. Once applied to a number of peaks, an average was taken for both single electron peak and total energy peak. For the single electron peak the average error was estimated to be $\pm$ 10 channels and for the total energy peak this was $\pm$ 28 channels. On average this gave the light yield an error of $\pm$1.6 phe/MeV, which is likely to be an over estimate.

## 3.4 Avalanche Photodiode Benchmarking

### 3.4.1 APD testing procedure

The HPS experiment requires 442 Large Area APDs, one for each of the $PbW0_4$ crystals. 74 additional APDs were purchased as replacements in case damage occurred during APD installation. Before the APDs could be coupled to $PbWO_4$ crystals, all 516 APDs needed to be tested to achieve a number of goals. The tests included measuring the APD dark and light currents at increasing voltages for multiple temperatures. The resulting analysis of these measurements allowed different checks. Initially the APDs were required to be tested to check that they functioned correctly. Noisy or malfunctioning APDs would be returned to the manufacturer or discarded. Once all functioning APDs were identified, they were arranged into different groups whose gain at the same applied voltage is approximately the same. The grouping is important as each HV power supply for the ECal has adjustable voltage for groups of 10 channels.

The APD tests were performed using a device built by INFN, shown in Figure 3.17. The APDs were installed on two printed circuit boards (PCBs) which have a blue LED in the centre. A blue LED was used as the peak emission of light is similar to that produced in $PbW0_4$ scintillation, allowing APDs to be tested under conditions similar to that expected within the experiment. 24 APDs can be fitted into the test rig at the same time, 12 around each LED. The APD dark current and intrinsic gain are dependent on temperature, hence the device is required to have a stable temperature. This was achieved by placing copper plates, connected to a chiller on top of the PCB. The copper plates had drilled holes to allow the APD pins to be connected to the PCB. The chiller circulated a refrigeration liquid that could vary in temperature between 22$^o$C and -6$^o$C. The voltage supply circuits and pre amplifiers were mounted on the PCBs. Plastic caps with reflecting foil were placed over each of the two boards to try and achieve light homogeneity for all 24 APDs. The whole system was placed in a light tight plastic box [33].

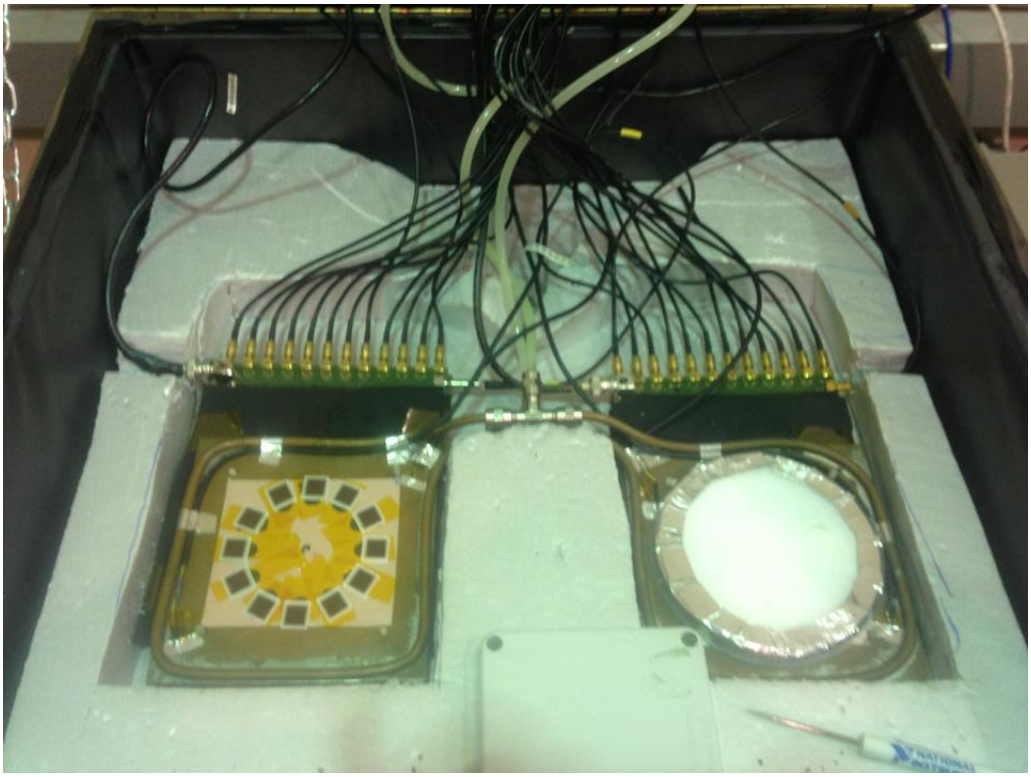

Figure 3.17: Large Area APD testing apparatus used to measure light and dark currents. On the left, 12 APDs are connected through the copper plates and around a blue LED. On the right, a reflector cap covers 12 connected APDs.

The tests comprised of measuring the internal gain of the Large Area APD as a function of the applied voltage (V) and temperature (T). The gain was determined using the relation below, see Equation 3.3. The dark current, $I_{off}^{led}$, and the current when the APD was exposed to LED light (light current), $I_{on}^{led}$, were measured at different values of applied voltages. $I_{off}^{led}$(G=1) and $I_{on}^{led}$(G=1) represent the light and dark currents when the avalanche process is not present in the APD, ie when the internal gain (G) is equal to 1 and the applied voltage is equal to 0 V [32].

$$G(V,T) = \frac{I_{on}^{led}(V,T) - I_{off}^{led}(V,T)}{I_{on}^{led}(G=1) - I_{off}^{led}(G=1)} \tag{3.3}$$

During the running of the tests, only one HV supply and one pico-amperometer (which measures the current) was used for the set-up, therefore only one APD could be tested at one time. The dark and light current was measured for each APD at three different temperatures, 20$^o$C, 18$^o$C and 16$^o$C. The full measurement at each

temperature takes ∼5 hours, therefore taking ∼ 15 hours for the full characterisation of 24 APDs. Full measurement of all 516 APDs was performed over several weeks at JLab. The system was controlled by Labview allowing the user to change temperatures and the HV for individual channels. The data was analysed using a ROOT macro, the procedure fully explained in the results section. Measurements would only be taken once the temperature had reached its selected value and then stabilised within $0.1^{o}$C.

### APD Dark current

Dark current describes the electric current that flows through the APD when no photons are present. The dark current is a combination of two different components, Equation 3.4: the bulk current $I_b$ and the surface current $I_s$ [32]. The bulk current depends on defects that create allowed energy levels in the band gap. The surface current is due to surface defects which are correlated to the fabrication of the device, i.e. etching and surface treatment.

$$I_d = I_b + I_s = I_b G + I_{s0} \tag{3.4}$$

The gain, $G$, is only dependant on $I_b$, which is the bulk current before multiplication. Therefore the dark current is expected to have a linear relationship with the APD Gain [32].

## 3.5 APD Benchmarking Results

### 3.5.1 Example APD results

The current was measured in steps of 5 V from 5 V to 50 V and again from 350 V to 410 V. Between 50 V and 350 V the current was measured in 50 V increments. The current was measured for both dark and light conditions at three different temperature 16$^o$C, 18$^o$C and 20$^o$C. Figure 3.18 shows the behaviour of the dark and light currents as a function of the applied voltage at T=18$^o$C. The red markers represent the dark current ($I_{off}^{led}$) and the black markers represent the light current ($I_{on}^{led}$). Typically the dark current is two orders of magnitude smaller than light current.

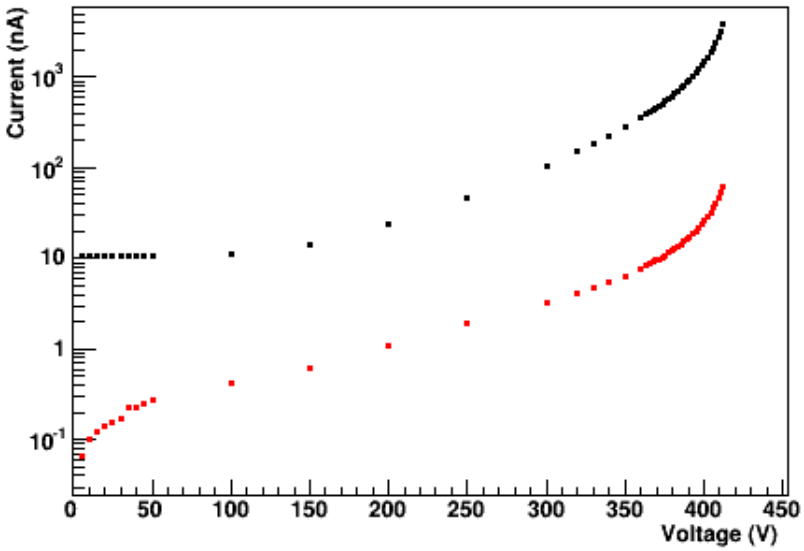


Figure 3.18: Light (black) and Dark (red) currents for one Large Area APD measured when temperature was 18$^o$C.

The small voltage steps below 50 V allow $I_{off}^{led}$(G=1) and $I_{on}^{led}$(G=1) to be calculated. This is achieved by performing a line of best fit to the current data below 50 V, see Figure 3.19. The intersection with the y-axis provides $I_{off}^{led}$(G=1) and $I_{on}^{led}$(G=1) values. Table 3.2 provides the $I_{off}^{led}$(G=1) and $I_{on}^{led}$(G=1) for all three temperatures and also the dark and light currents at 400 V. The small voltage increments at higher voltages yields detailed information around the working voltage of the APD.

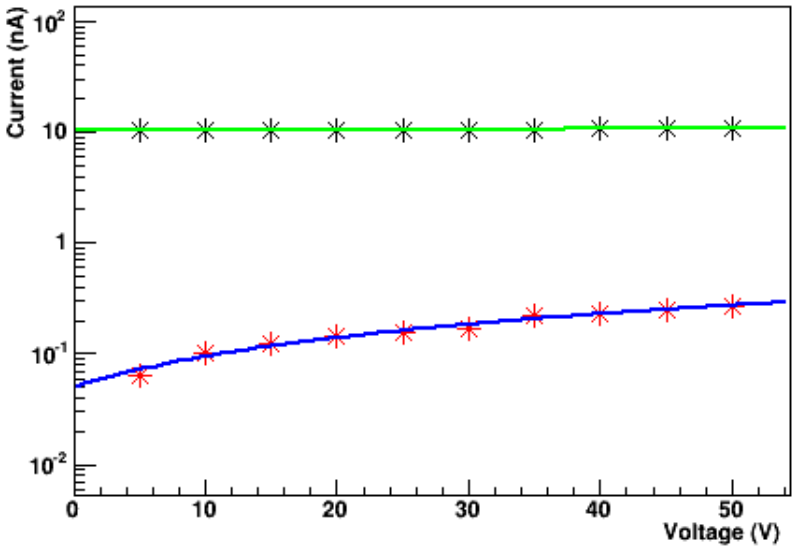


Figure 3.19: Light (black) and dark (red) currents measured in small steps of 5 V for one APD at T=18$^o$C. A linear fit was performed to extrapolate the light and dark current when G=1, which is equivalent to zero applied voltage.

Table 3.2: Light and Dark current measurements: G=1 currents determined for the linear fit and the current values at an applied voltage of 400 V are taken from the data points

| | 20$^o$C | 18$^o$C | 16$^o$C |
|---|---|---|---|
| $I_{off}^{led}$(G=1) (nA) | 0.067±0.009 | 0.049±0.007 | 0.052±0.008 |
| $I_{on}^{led}$(G=1) (nA) | 11.320±0.007 | 10.470±0.008 | 9.516±0.004 |
| $I_{off}^{led}$(400 V) (nA) | 26.716±0.006 | 26.955±0.007 | 23.323±0.004 |
| $I_{on}^{led}$(400 V) (nA) | 1476.730±0.004 | 1485.470±0.008 | 1793.740±0.006 |

The dark current is predicted to decrease as the temperature decreases. Within uncertainties this is true for the APD 228 which was tested, if measurements were made over a wider range of temperatures this trend would be more visible [32]. However the measured light current at 400 V shows a clear increase at lower temperatures, which is also expected. Using these values and Equation 3.3 the gain was calculated giving G(400 V,20$^o$C) = 128.86, G(400 V,18$^o$C)= 139.97 and G(400 V,16$^o$C)= 186.15. This clearly demonstrates that the gain is strongly dependant on temperature and decreasing the temperature of the APD increases the gain. Comparing the

dark and light currents in Table 3.2 also supports the expectation that there should be a two order of magnitude difference between the two, which gives us a criterion for the quality of the APD performance. Figure 3.20 shows the calculated gain at all applied voltages for APD 228 at T=18$^o$C.

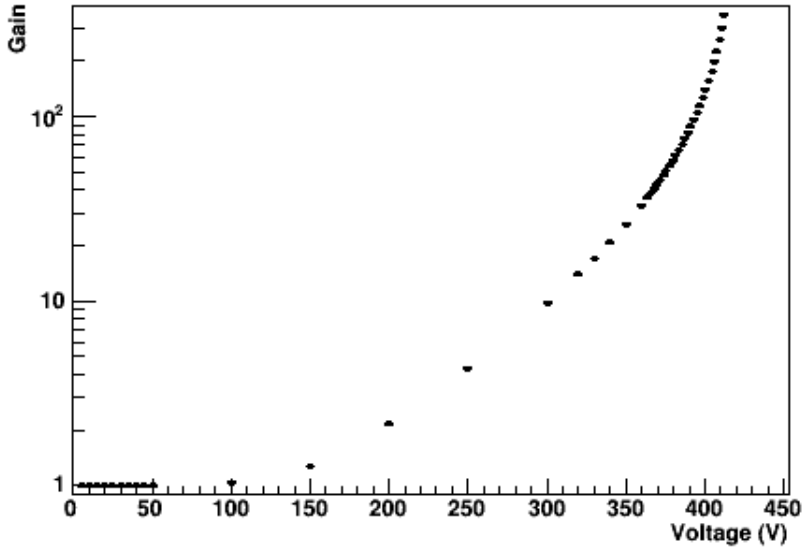


Figure 3.20: The APD gain as a function of applied voltage at 18$^o$C

Using the measurements from all three temperatures a three dimensional gain map can be created as as a function of applied voltage and temperature. Figure 3.21 is the 3D gain map for APD 228. The colour chart represents the different values of gain and the solid curved lines represent values of equal gain.

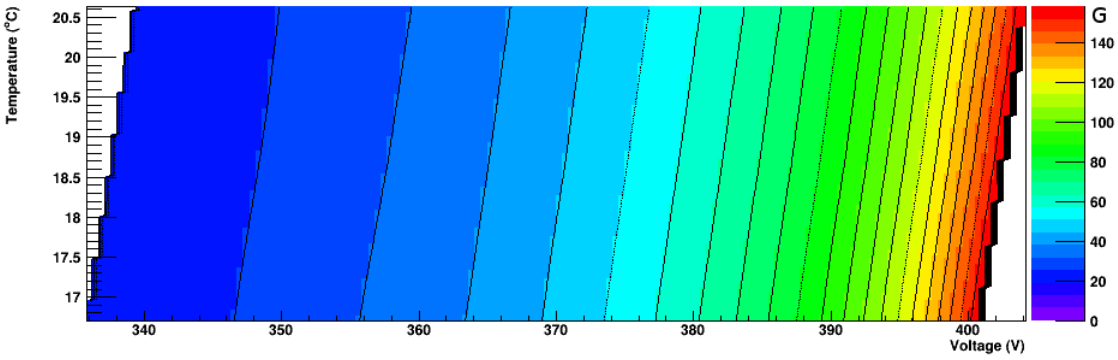


Figure 3.21: A 3D gain map as a function of applied voltage and temperature, for one APD.

This clearly shows the dependence of gain on temperature. For one gain value

achieved at 20$^o$C, the same can be achieved at a lower temperature and at a lower applied voltage. This relationship can be expressed as a linear combination of temperature and voltage:

$$G(V,T) = G(\alpha V - \beta T) \tag{3.5}$$

Where $\frac{\alpha}{\beta}$ is the common slope of the straight lines of equal gains and the multiple of G represents the lines of constant gain presented in Figure 3.21. Performing a simple differentiation on Equation 3.5 provides the following relations which describe the relative dependence of gain for temperature and voltage:

$$\alpha = \frac{1}{G}\frac{\partial G}{\partial V} \tag{3.6}$$

$$-\beta = \frac{1}{G}\frac{\partial G}{\partial T} \tag{3.7}$$

Specifically, $\alpha$ supplies important information about the functionality of the APD. It describes the variation of the gain with respect to the applied voltage, normalised to the gain. Figure 3.22 shows the $\alpha$ versus gain plots for the three temperature measurements. Since $\alpha$ is not dependant on temperature, the three $\alpha$ plots determined using G(V,T$_i$), where T$_i$=$\{$20$^o$C, 18$^o$C, 16$^o$C$\}$, should fall on the same trend when superimposed, as shown in the figure. If they do not follow the same trend, this is an indication that the APD is not functioning correctly.

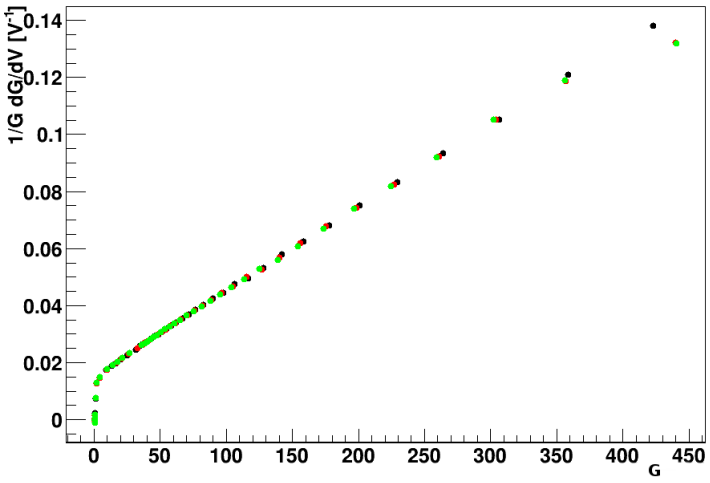


Figure 3.22: $\alpha$ as a function of gain for all three temperature measurements, when superimposed should follow the same trend as $\alpha$ is not temperature dependant. Black, red and green markers represent the measurements taken at 16$^o$C, 18 $^o$C and 20$^o$C respectively.

Finally, it is important that the dark current follows a linear trend as the gain increases, explained by Equation 3.5. This is proven to be true for APD 228, from a plot of the gain vs. the dark current, see Figure 3.23.

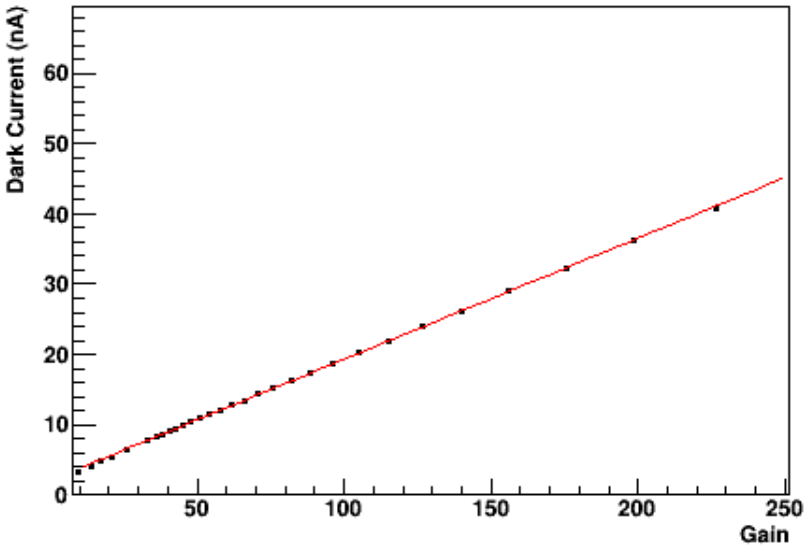


Figure 3.23: The APD Gain and dark current follow a linear trend, as predicted by Equation 3.5.

### 3.5.2 Collective APD results

The results from the previous section are for one APD, 516 were tested in total. Each day after measurements were completed, each of the plots from above were visually checked by the user.

- The first check was the light and dark current measurements for each of the temperatures, Figure 3.18. The current measurements were mandatory for a successful run as progressive analysis was dependant on this data. If any current measurements were missing the APD was retested.

- If all current measurements were present the next check was of the magnitude of dark current compared to the light current. Typically for a good APD, the dark current is two orders of magnitude smaller than the light current. Initially an APD that did not fill this criteria was not yet considered to be a noisy APD. The effect could be due to systematic errors within the set-up of the experiment (stray currents) therefore the APD was retested.

- The next step was to check that $\alpha$ for each temperature followed the same trend when the graphs were superimposed. If this was not the case, the APD was retested for all 3 temperatures.

- The final check was the distribution of dark current for increasing gain. This is expected to be linear. Deviations within a few percent were still viewed as a "good" APD, however APDs with a higher deviation were retested.

If the APDs fulfilled the conditions above they were identified as functioning APDs with a sufficiently low noise level. If after retesting the results did not improve the APD would be discarded or replaced by the manufacturer.

One final check that was performed was to determine if any malfunctioning APDs were missed. This involved comparing measured data to data provided by the manufacturer, Hamamatsu. Hamamatsu provided the voltage at a gain of 150 measured at T=18$^o$C for each APD. Figure 3.24 is a the comparison of the measurements made using the INFN apparatus and the measurements provided by Hamamatsu. There is a clear correlation between the two, with a small offset that could be due

to systematic errors arising from differences in measurement technique . The measurement technique for Hamamatsu is unknown. However there are a few major outlying points, the APDs corresponding to these points were retested.

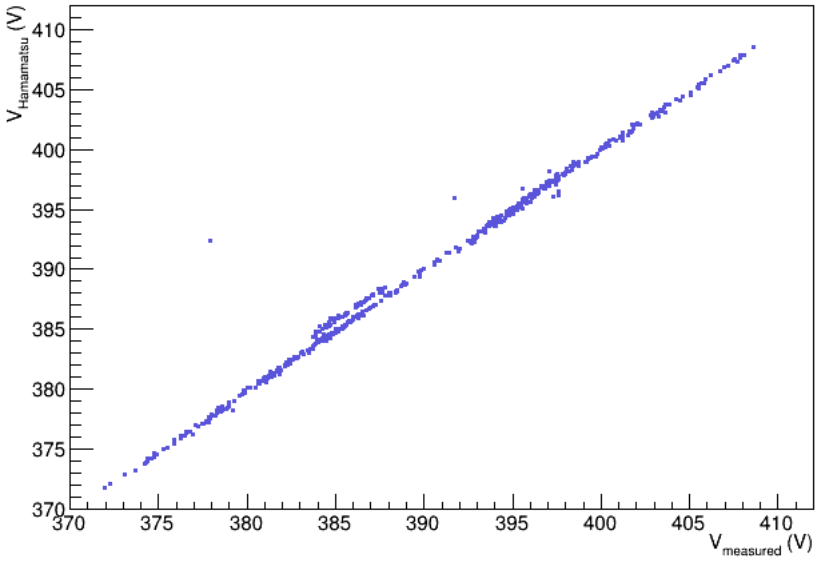


Figure 3.24: The applied voltage at 18$^o$C and gain 150 using the INFN set-up compared to values measured by Hamamatsu at the same temperature and gain. Any major outlying points were retested.

For the HPS experiment fortunately all APDs functioned within the requirements of the experiment and none of the 516 APDs had to be discarded or replaced by the manufacturer.

### 3.5.3 HV Grouping

The High Voltage (HV) power supplies for the HPS experiment have 10 available channels, hence powering 10 APDs per power supply. Ideally since one voltage is set for each power supply, the APDs in each HV supply group should have similar working voltages at a set gain and temperature. From the APD testing detailed in Section 3.4.1 all the APD data was collected and grouped into a global plot. The global plot is the distribution of the APD applied voltage at a set gain of 150 measured at T=18$^o$C, shown in Figure 3.25. Due the shape of the ECal, 30 groups of 10 APDs were required in total, the rest of the groupings were sets of 9, 8, 7, 6,

5, 4. The individual groups were created by making cuts in the global plot. From this, each group would have a similar applied voltage, produce a gain of 150 at a temperature of 18$^o$C, the proposed running temperature of the ECal. A successful grouping had an RMS voltage less than 0.5 V.

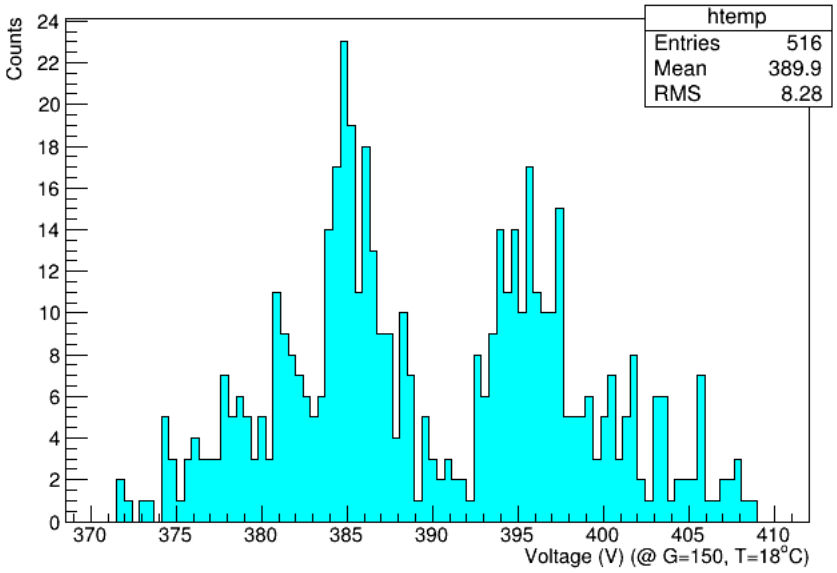


Figure 3.25: A global plot of all 516 APDs, showing the distribution of applied voltages that produce a gain of 150 at T=18$^o$C. From this, the HV grouping was allocated by making cuts in the plot, to select APDs with a similar voltage.

## 3.6 Light Emitting Diode Tests

### 3.6.1 LED Irradiation tests

Previous experiments have used LEDs in their light monitoring system, however the light is often directed along fibre optic cables to the crystals from a source not within reach of the beam line. For example the system developed for the BTeV calorimeter at Fermi National Accelerator Facility [38] used two independent red and blue LEDs and fibre optic cables to transport light to the crystals. However, few experiments have used LEDs that have been directly coupled to the face of the crystals. The CLAS12 Foward Tagger calorimeter (FT-Cal) [32] and PANDA experiment [31] are currently developing this method. The HPS Light Monitoring System (LMS) is predominantly based on the FT-Cal design. Due to this method only recently being implemented, there is no known documentation on how the LEDs behave after exposure to high levels of electromagnetic radiation.

During crystal irradiation tests at the University of Giessen, 10 LEDs were exposed to the same $^{60}$Co source. Using the MAS 40 Mini-Array Spectrometer the wavelength and intensity of the LEDs was measured. Measurements were taken for both LED colour settings before and after irradiation. The LEDs received the same dose as the crystals, 30 Gy.

### 3.6.2 LED Irradiation Results

The spectrometer measured the emitted light intensity of the LEDs and the peak wavelength. Figure 3.26 and Figure 3.27 are examples, for one LED, of emission spectra before and after irradiation for both the blue and red settings. There appears to be no significant damage when the two emission spectra are superimposed. The average mean peak wavelength of the LEDs were measured as: $\lambda_{blue} = (467.5 \pm 1.8)$ nm and $\lambda_{red} = (638.7 \pm 1.5)$ nm.

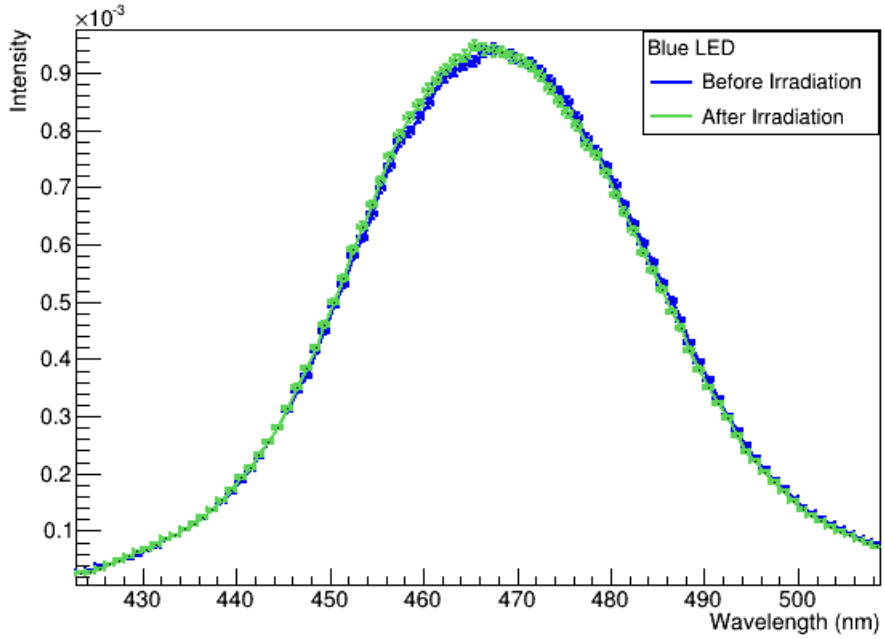


Figure 3.26: Blue LED emissions spectra, for before (blue) and after (green) irradiation. No significant damage is seen.

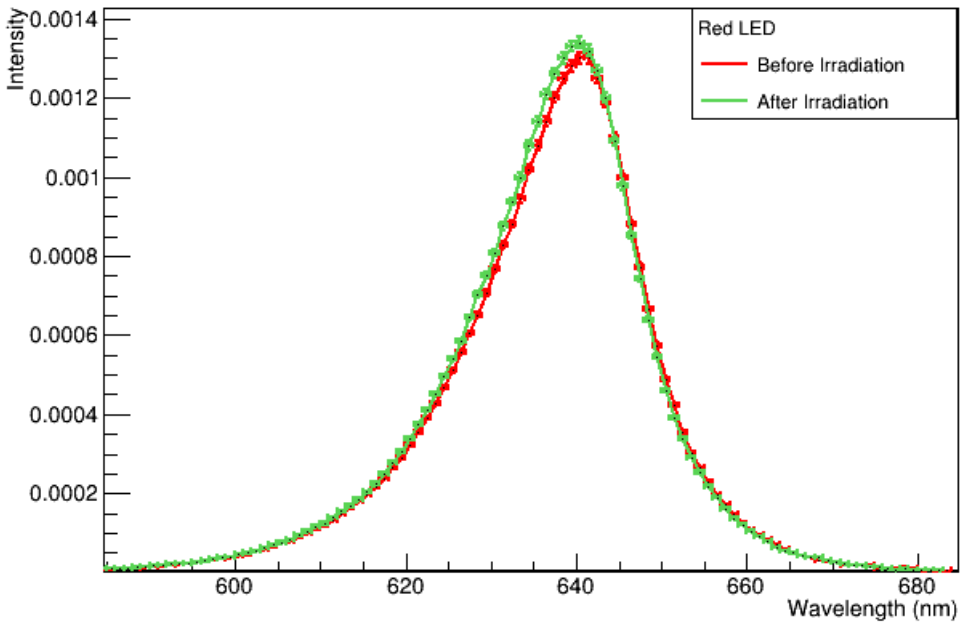


Figure 3.27: Red LED emissions spectra, for before (red) and after (green) irradiation. No significant damage is seen.

To quantify the damage, a Gaussian was fitted to each of the emission spectra and the difference between the mean peak wavelengths was calculated for both

colours, see Figure 3.28. The differences in wavelength are within a few nm. This is a relatively small deviation which is likely to be a systematic error in the measurement. It is also possible that these are associated differences in the $\lambda$-distribution for different emission angles. The LEDs have a directivity of 30 degrees, where directivity refers to the change in light intensity on the variation of angle from a central axis. [42]. Therefore slight differences in the LED positioning can lead to the light being directed to the photodiode within the spectrometer at a slightly different angle, which may also explain the differences in the peak $\lambda$. The manufacturer of the spectrometer states that the accuracy of the wavelength measurement is $\pm 0.5$ nm and 1% accuracy in the intensity. The differences in the intensity between the two measurements was not quantified, however, visibly looking at the emission spectra for both colours no significant differences can be seen.

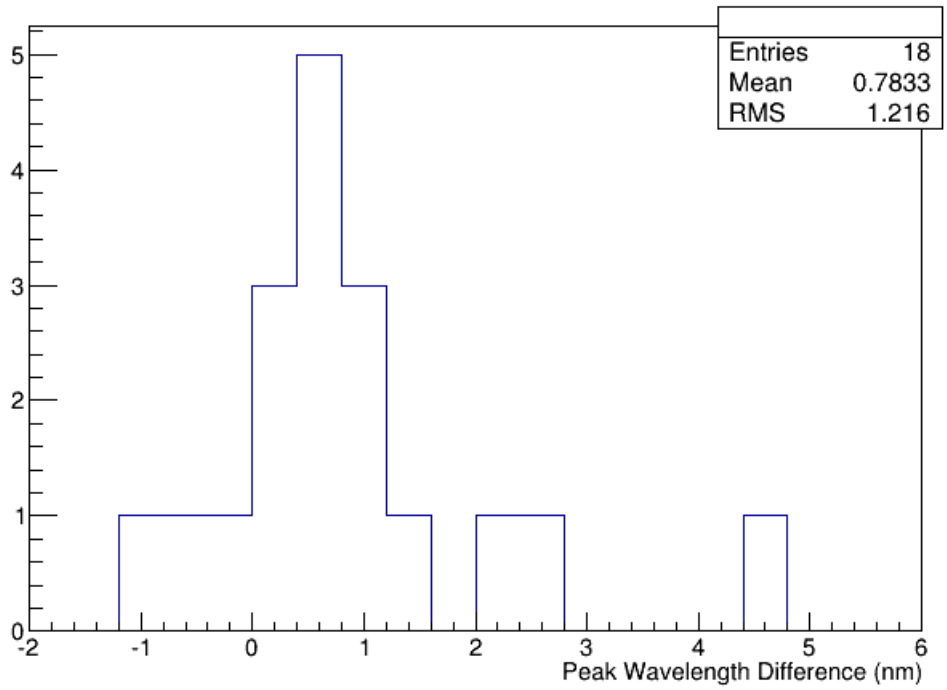


Figure 3.28: Difference in mean peak wavelength measured before and after irradiation.

From this, the deviations in mean peak wavelength are thought to be due to positioning and systematic errors in the measurement and not due to irradiation

damage effects. Therefore, large deivations in the mean peak wavelength of the LED are not expected over the course of the HPS experiment due to electromagnetic radiation.

### 3.6.3 LED Characterisation

The Light Monitoring System LEDs are required to pulse at high frequencies. This is an uncommon requirement for LEDs are they are often used as a continuous light source or flashed for longer time periods than $\backsim$100 ns. Therefore before the LEDs could be wired to the connection boards each LED was tested to determine if they functioned within certain characteristics. 600 bi-coloured LEDs were purchased in total to allow for spares. The specifications were: at the maximum pulse amplitude before saturation the pulse amplitude must be between 2 V - 3 V and the pulse width must be less then 150 ns, to obtain sufficient light output and a sharp enough pulse. This pulse width specification was required to be less than 150 ns so that the pulse would be similar in characteristics to a scintillation photon produced in $PbWO_4$.

The LEDs were tested using a set-up that was a prototype of what would eventually resemble the LMS. The set-up included a light-tight hollow aluminium tube with a Large Area APD and corresponding amplifier at one end and an opening for an LED at the other, see Figure 3.29. Copper tubing was wrapped around the aluminium rod with chiller attachments at each end. Water was circulated through the attachments and copper tubing by a Huber machine which regulated a constant temperature of $18^oC$. An LED was placed inside the gap which had a screw attachment to minimise outside light exposure. The LED was powered by a PCB circuit board which was controlled by a computer though a USB connection. The PCB pulsed the LED at different frequencies and amplitudes. An oscilloscope was connected to display the measured signal from the APD. The LED PCB was powered by a +12 V power supply and the APD required +400 V HV power supply and an additional +5 V,-5 V for the pre-amplifier.

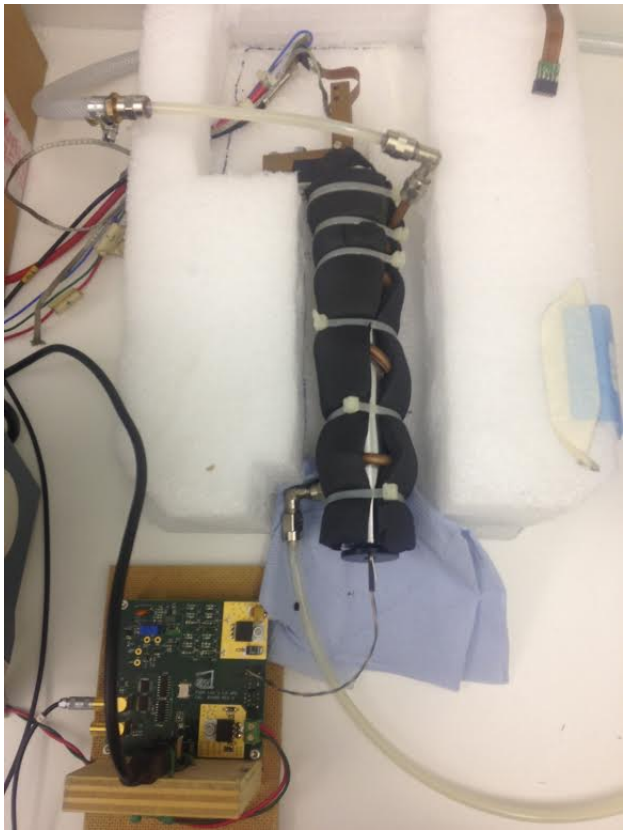

Figure 3.29: The LED characterisation set-up used to determine if the LED produced a pulse within set specifications. An APD measured the light pulse sent from an LED at the other end of a light-tight aluminium rod, which was maintained at a temperature of 18$^o$C. The pulse was displayed on an oscilliscope.

### 3.6.4 LED Characterisation Results

To determine if the LED met the specifications, the measured pulse amplitude was manually checked on an oscilloscope. Built-in oscilloscope settings allowed the pulse amplitude to be measured and displayed on the screen. However, there was no equivalent setting for the pulse width therefore the pulse width was estimated by identifying markers on the screen as reference points and reading the scale by eye. The electrical signal driving the LED is much shorter than the final signal width as the LED response is significant smaller. Figure 3.30 is an example the pulse measured from a red LED.

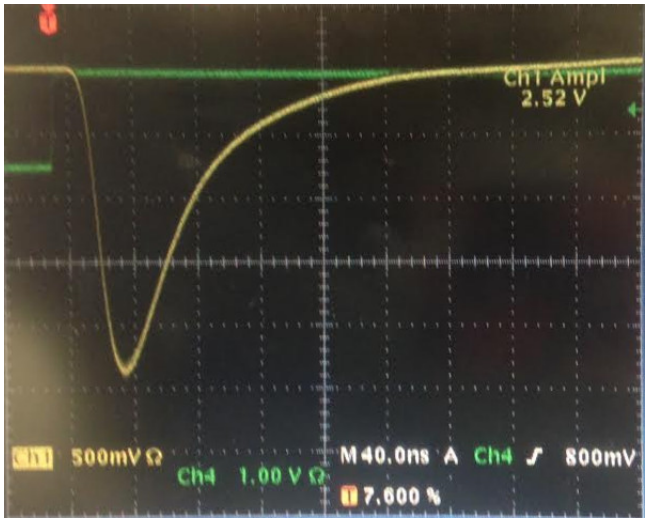


Figure 3.30: Example red LED pulse as seen on an oscilliscope.

The first 50 LED measurements were recorded. The spread of the pulse amplitudes are shown in Figures 3.31(left) for the red LEDs and Figures 3.31(right) for the blue LEDs. On average the pulse amplitude was $\sim$ 2.5 V and the ratio of the pulse amplitudes measured for each colour was around about $\sim$1, shown in Figure 3.32.

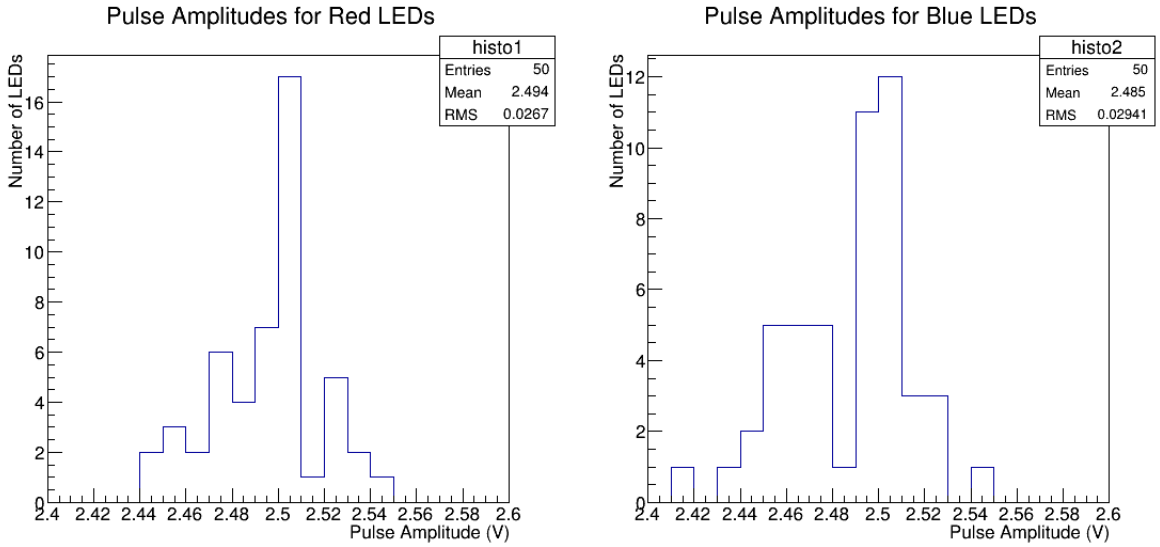


Figure 3.31: The distributions of the measured pulse amplitudes for the red (left) and blue (right) LEDs.

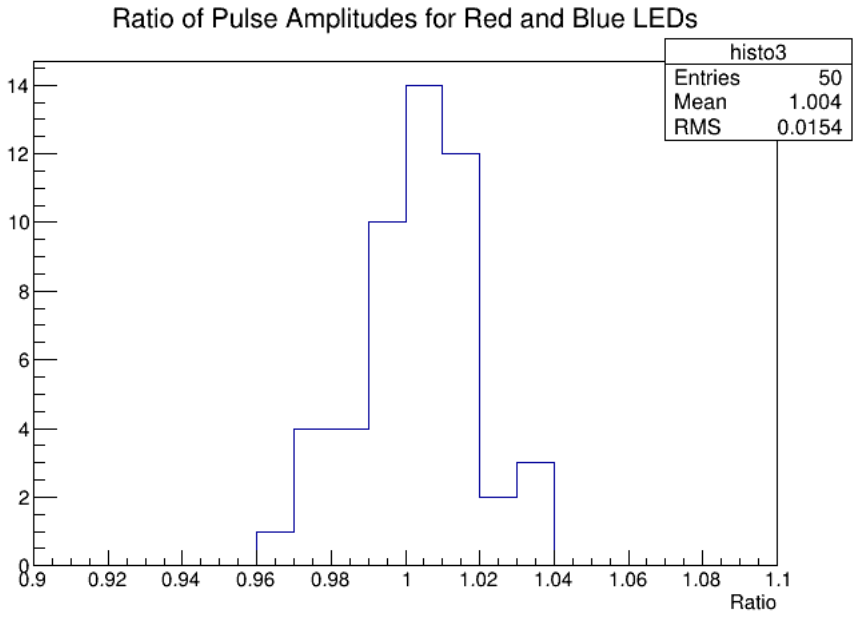


Figure 3.32: Ratio of the red and blue pulse amplitudes for each LED.

All LEDs were tested for each colour setting and were found to have a pulse amplitude between 2 - 3 V. All pulse amplitudes measured on the blue setting had a pulse width less than 150 ns, however this was not true for the red setting. Almost 100 LEDs were set aside as they had a red pulse width greater than 150 ns. Since most were close to 150 ns and the measuring technique of the pulse width is estimated by eye these LEDs were initially not excluded. They were kept as spares in case LEDs were damaged during the installation process.

# Chapter 4

# ECal Assembly

## 4.1 CLAS Inner Calorimeter

The HPS Ecal was constructed using recycled parts from the previous Inner Calorimeter (IC) for the Deeply Virtual Compton Scattering (DVCS) Experiment, also Hall B, JLab. The IC consisted of 424 $PbWO_4$ crystals arranged in an octagonal shape, see Figure 4.1. An example individual IC module is shown in Figure 4.2. At one end of the crystal, an optical fibre connector is glued to the VM200 wrapping of the crystal. At the other end is an APD with an active region of 5x5 $mm^2$ which was previously glued using an optical cement. The remaining area of the face of the crystal was sealed with silicone to make the crystal light-tight. The APD is attached to the pre-amplifier and corresponding electronics.

Recycled IC parts used in the HPS ECal were the $PbWO_4$ crystals and aluminium support frames. The IC was completely disassembled and a few changes were made before the new HPS ECal configuration was constructed. The changes included removing the original 5x5 $mm^2$ APDs and optical fibre holders, this was achieved using a number of different removal and cleaning techniques. Once completed the new Large Area APDs and LED holders were attached in preparation for the new HPS ECal being built.

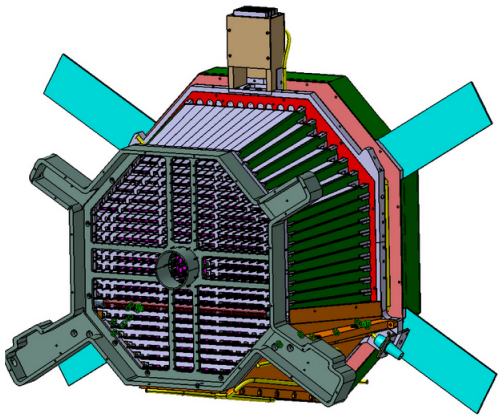

Figure 4.1: The design of the HPS ECal was based on using recycled $PbWO_4$ and aluminium support frames from the previous DVCS experiment's Inner Calorimeter.

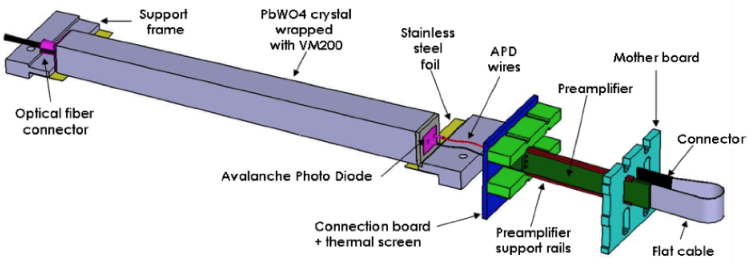


Figure 4.2: An IC module consisting of a $PbWO_4$ crystal, an optical fibre holder, a 5x5 $mm^2$APD and pre-amplifier.

## 4.2 Dismantling and Preparation

The crystals were initially attached to the aluminium frames using silicone. To remove them, blunt plastic knifes and force was used. The fibre optic end-caps were detached using a scalpel, being careful not to damage the VM200 wrapping. The end caps were purposely attached to the wrapping and not the face of the crystal, however if previously glued incorrectly, part of the crystal would be removed with the end-cap. To remove the APDs the crystals were heated in an oven set to $80^oC$ for at least an hour. This heat softened the optical glue allowing the APD to be removed by pulling at the two pins using pliers. Excess glue was removed using a soft lint-free cloth. The oven was then switched off and the vents opened. The were

crystals were then placed back into the oven and left to cool down gradually for around 2 hours or until the oven temperature was below $40^oC$.

The majority of the crystals had the silicone layer and excess glue still attached after the APDs were removed. Initial cleaning methods included using wooden utensils, plastic knives and plastic q-tips with ethanol. However some of the methods caused damage to the crystal and wrappings. Dependant on the wooden utensils used, scratches could occur on the surface of the crystal. As the silicone was difficult to remove, often if too much pressure was applied the wrappings could tear. To try and avoid damage and quicken up the cleaning process, the crystals were placed in an ethanol bath for around 1 hour. After one hour of exposure to the ethanol the silicone could be more easily removed using a blunt wooden stick leaving minimal silicone behind. Leftover silicone was removed using a combination of a blunt plastic knife and q-tips with ethanol.

The process of removing the APDs and the end caps often caused some damage to the wrapping. In some cases this only involved correcting the tears with a reflective tape, though sometimes the crystals needed to be re-wrapped completely. Figure 4.3 is an example of each of the different crystal cleaning stages.

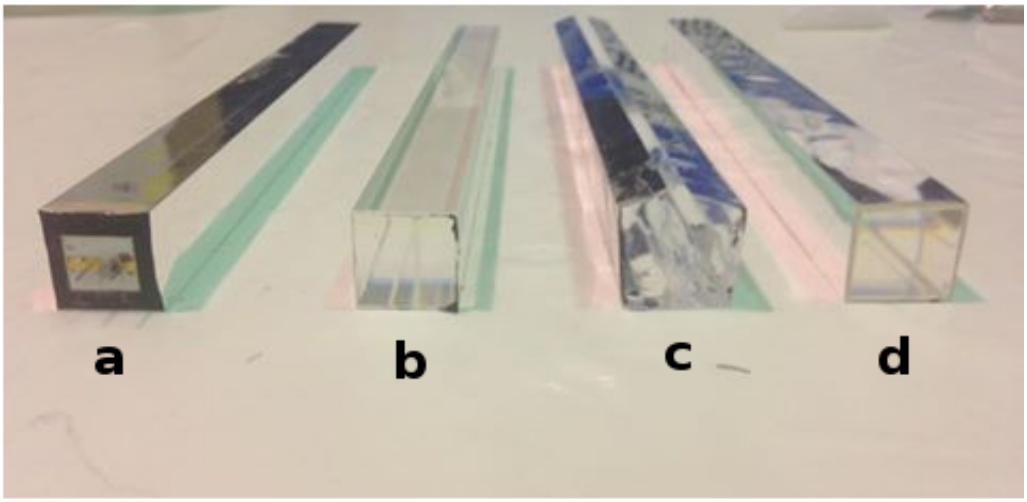


Figure 4.3: (**a**)crystal with original APD and silicone still attached, (**b**) crystal after APD, wrapping and majority of the silicone removed, (**c**) New VM200 wrapping, (**d**) Crystal re-wrapped and ready for new large area APD and LED end-cap

Some damage caused the crystal be completely unusable, however, due to spare crystals from the IC there was enough $PbWO_4$ to construct the ECal.

## 4.3 HPS ECal Assembly

### 4.3.1 APD gluing

The Large Area APDs were glued to the crystals using a device that exploited the weight of the crystal. Ten APDs could be glued at one time using devices built by INFN Genova, see Figure 4.4. The white bottom section held the APD, it had an imprint of the APD pins and dimensions to securely hold the APD in place. The upper grey section held the crystal, moveable plastic screws were adjustable to ensure that the crystal was held upright and stable. Large metal screws attached the two pieces together from the bottom. The first step of gluing the APDs was

dismantling the set up into two parts. An APD was then placed into the holder. The APD was then lightly cleaned with a cotton bud soaked in ethanol. A small amount of optical glue was then placed on the active region of the APD and the crystal was placed into the upper grey section. The two parts were then connected and secured with the screws on both the bottom and upper parts. This was repeated for all 10 crystals. The device was left in the vertical position for at least 12 hours.

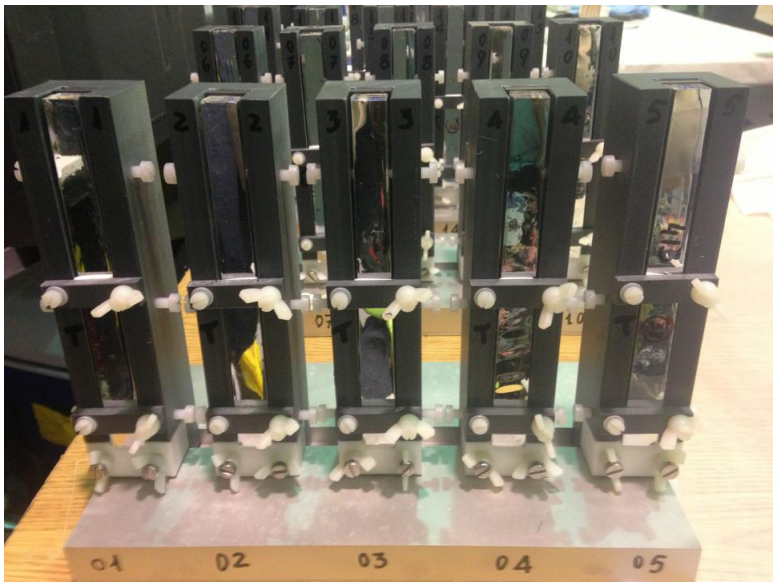


Figure 4.4: APD gluing set-up.

After 12 hours the crystal was carefully removed from the device. To check if the APD had been successfully glued, the APD was check by looking through the crystal from the other end. Any identifiable bubbles on the active region was noted so that further checks could be made. Figure 4.5 is a picture of APDs successfully attached to the crystals.

Figure 4.5: A set of APDs glued to the $PbWO_4$ crystals.

### LED Endcaps

Figure 4.6 is a picture of the LED end-caps, where a small hole was later punched in the centre to convey the LED light. Each cap was attached to the front face of each $PbWO_4$ crystal using a small amount of optical glue on each corner.

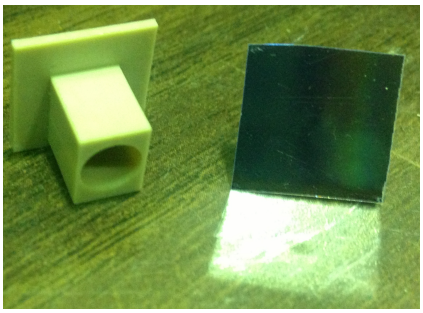

Figure 4.6: LED endcap

Once the APDs and LED end-caps were attached to the $PbWO_4$ crystals they were placed back onto the aluminium support frames also recycled from the DVCS IC, see Figure 4.7.

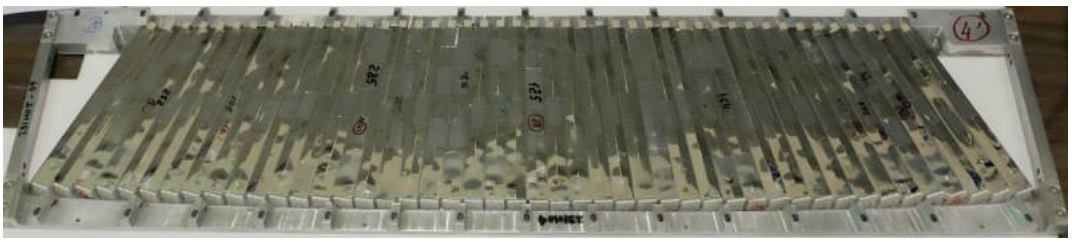

Figure 4.7: One layer of the ECal with the recycled $PbWO_4$ crystals and the new Large Area APDs and LED end-caps.

## 4.3.2 Light Monitoring System Cross-Talk

During the initial installation of the Light Monitoring System, each channel was tested to determine if the LEDs and APDs were working and that all the cabling matched up. This was achieved by looking at the LED light pulses measured by an APD on an oscilloscope. During this procedure a cross-talk was observed between neighbouring crystals, where cross-talk is when an LED is switched on for one crystal and the APDs in the surrounding crystals measure a signal. This observation

suggested that each of the crystals were not individually light tight.

To quantify the cross-talk and determine potential sources of escaped light, 4 different crystal positions were chosen on one ECal layer to see if the geometry changed the measured signal. The cross-talk was measured by switching on one of the LEDs and measuring the signal in the corresponding APD shown on an oscilloscope. With the LED still switched on the signal was measured again in all 8 surrounding APDs above, below and next to the active crystal. The measurements were taken at room temperature without the chiller attached. The red LED setting was pulsed at a frequency of 1 kHz and the HV supply was set to 390 V for the APD. Figure 4.8 is a picture taken while the LMS was being installed to the top half of the ECal. Each stacked layer of crystals is visible on the right and one installed connection board for the LMS is seen on the left.


Figure 4.8: Top half of the ECal during LMS installation. Stacked layers of crystals can be clearly seen on the right and one connection board of the LMS is installed on the right.

### Cross-talk Results

Figure 4.9 is a schematic diagram of one layer of the ECal, the four crystals tested are highlighted in red. Positions (a) and (b) were both tested as there is a vertical metal rod between the two. The LEDs are at the top and the APDs are at the bottom of the diagram.

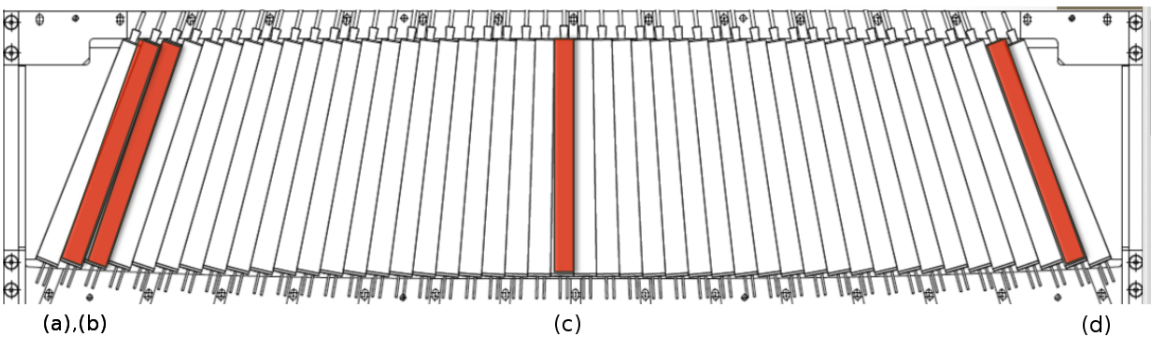


Figure 4.9: Schematic Diagram of one layer of the ECal. The red highlighted crystal are the ones where the LED was switched on and the surrounding APDs were tested to see if a cross-talk was measured. Each crystal position is labelled: (a),(b),(c) and (d) which correspond to the cross-talk results given in Table 4.1.

Figure 4.10 is an example of the different signals measured by the oscilloscope: (a) is the LED signal measured in the APD corresponding to the LED switched on. (1.85 V), (b) is a signal when cross-talk was observed and (c) is a noise signal.

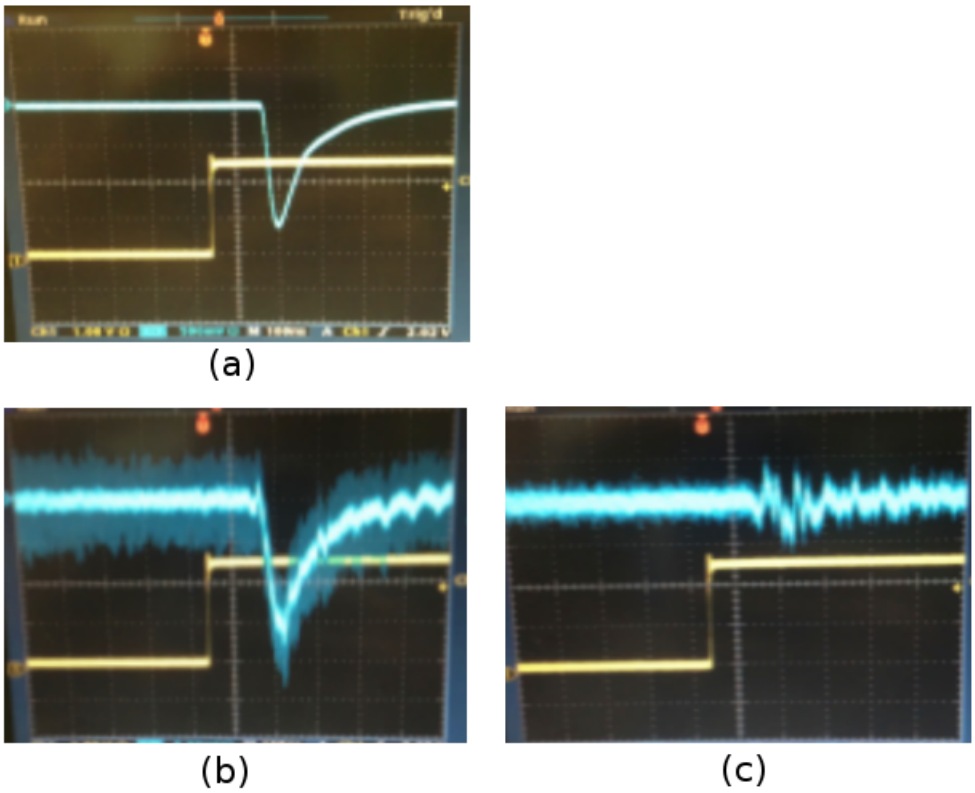


Figure 4.10: (a) is the signal measured in the APD corresponding to the LED switched on, (b) is the signal measured in neighbouring APDs on the same ECal layer and (c) is a noise signal. The oscilloscope scale for measuring the LED signal was between 200-500 mV per division and 5 mV when measuring the cross-talk or noise.

The pulse amplitude measured in the APD corresponding to the LED switched on was 1.85 V. Noise signals were measured in the APD channels on layers above and below the chosen ECal layer tested. However there was a clear signal measured in the two neighbouring APDs on the same layer, see Figure 4.10(b). Table 4.1 displays the measured pulse amplitudes for each of the neighbouring APDs on the left and right side of each of the positions in Figure 4.9. In the brackets is the percentage of the signal measured in these APDs from the original signal pulse amplitude (1.85 V).

Table 4.1: The cross talk measured in the neighbouring APDs of the positions described in Figure 4.9, for APDs on the same level. Displayed as both pulse amplitude (V) measure in the a neighbouring APD and the percentage with respect to the original signal pulse amplitude.

| Left Pulse Amplitude (V) | APD tested | Right Pulse Amplitude (V) |
|---|---|---|
| 0.029 (1.57%) | (a) | 0.048 (2.59%) |
| 0.022 (1.19%) | (b) | 0.039 (2.11%) |
| 0.057 (3.04%) | (c) | 0.021 (1.14%) |
| 0.040 (2.22%) | (d) | 0.019 (1.05%) |

The cross talk measured is greater for channels on the right side for (a) and (b) and greater for channels on the left of (c) and (d). The error on the measurements is 1%. It is easy to assume that the light is escaping from the APD side as the APD does not cover the full face of the crystal and silicone was not used to make the face light-tight, whereas on the other end the LED end cap is glued to the crystal and has the same dimensions as the crystal face. This warranted more investigation, however, as the magnitude is small, it was decided not to proceed as it would be impractical to dissemble the ECal to determine where the light was escaping for each individual crystal. The cross talk will be taken into account during the calibration of the ECal.

### 4.3.3 Current Condition of the ECal

As of September 2014, the ECal is full constructed and ready to be installed into the experimental hall in parallel with the other HPS Detector components . Figure 4.11 and 4.12 are recent pictures of the top and bottom sections of the ECal.

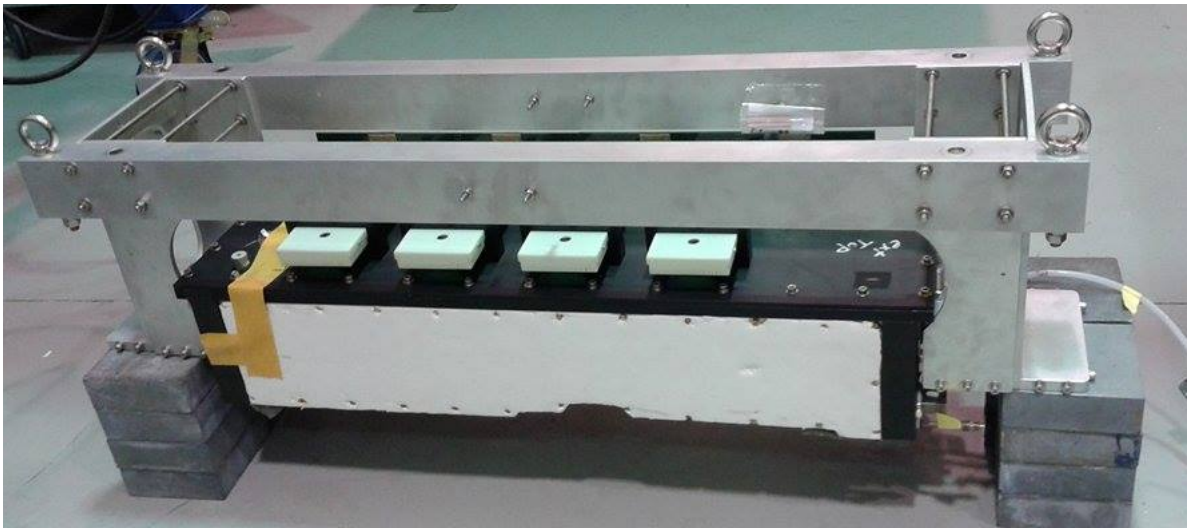

Figure 4.11: The top section of the ECal, fully constructed and ready to be installed into the experimental hall.

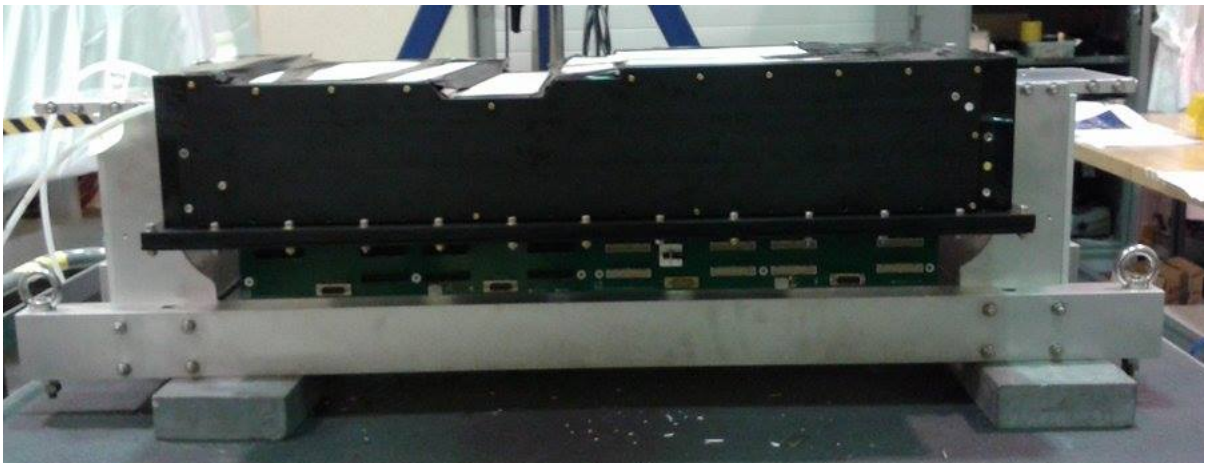

Figure 4.12: The bottom section of the ECal, fully constructed and ready to be installed into the experimental hall.

# Chapter 5

# Discussion and Conclusion

The ECal components were tested and the detector was constructed over the period March - September 2014.

Studies performed on the BTCP crystal found that scintillation crystals experience radiation damage from exposure to gamma-ray radiation. The damage lowered the overall longitudinal light transmission as a result of the formation of colour centres. In comparison to a crystal produced by SICCAS, the BTCP crystal had a better tolerance to radiation. However both crystals were successfully annealed using a blue LED light source from the LMS. This greatly reduces the recovery time compared to spontaneous relaxation which occurs naturally at room temperature, but on a time scale much greater than optical bleaching, which makes it impractical during the experiment. The measurement of the radiation induced absorption coefficient could have been repeated for multiple BTCP crystals to determine if the radiation hardness varies for crystals produced by the same manufacturer. From this, if a large deviation does occur, crystals with a the better radiation hardness could be placed closer to the beam-line and crystals with a lower radiation hardness, in comparison, being placed further from the beam-line. Due to time constraints, and the location of the crystals (JLab) and the spectrophotometer (Giessen) this could not be carried out.

Measurement of the SICCAS $PbWO_4$ crystal's light yield demonstrated that the light yield produced could be increased by decreasing the temperature. The SICCAS temperature coefficient measured is comparable with light yield measurements on

the PANDA $PbWO_4$ crystals. The light yield of the HPS BTCP crystal is expected to be similar to the light yield of the SICCAS crystal and the light yield measured at $18^oC$ was regarded to be adequate for the requirements of the HPS experiment.

The investigations performed on the APDs characterised the temperature dependance of gain and found a linear relationship as a function of temperature and voltage. The ECal High Voltage supply settings will be selected to provide the optimum APD gain. All of the APDs purchased from Hamamatsu were found to function within the requirements of the experiment and have an acceptable noise level.

Each bi-coloured LED will be coupled to the front face of each crystal. From the LED irradiation studies there was no noticeable difference in the LED light output due to damage caused by exposure to a $^{60}Co$ gamma-ray source. Therefore the light output is not expected to change due to the high levels of electromagnetic radiation produced over the course of the HPS experiment.

The characterisation tests performed on each bi-coloured LED found that the majority met the specifications of the LMS. All blue LED settings met both the pulse amplitude and pulse width requirements, however, this was not true for all of the red LED settings. All of the red LED settings produced a pulse amplitude within the requirements, but $\sim 100$ had a greater pulse width. However due to the uncertainly in the width measurement the LEDs were not discarded but kept in case damage occurred during the installation of the LMS.

The DVCS Inner Calorimeter was successfully disassembled using a series of removal and cleaning techniques. The HPS ECal was constructed using the recycled $PbWO_4$ crystal and aluminium frames and the new additional detector components. During the installation of the LMS, a cross-talk was observed. The source of the cross-talk was uncertain, however, due to the its small magnitude, it was decided that the investigation would not be taken further. If the cross-talk is due to escaped light, the light-tightness of the crystals could be improved using silicone to cover the exposed crystal around the APD, similar to the original Inner Calorimeter set-up. However due to the time constraints this could not be performed.

The ECal is currently ready to be installed in the experimental hall with the

other HPS detector parts. The installation is planned to start October 2014 and the first experimental run is proposed to begin November 2014.

# Glossary

ΛCDM Lambda Cold Dark Matter.

**ALICE** A Large Ion Collider Experiment.

**AMS** Alpha Magnetic Spectrometer.

**APD** Avalanche Photodiode.

**APEX** A' Experiment.

**ATIC** Advanced Thin Ionization Calorimeter.

**BTCP** Bogoroditsk Technical Chemical Plant.

**CAPRICE** Cosmic AntiParticle Ring Imaging Cherenkov Experiment.

**CEBAF** Continuous Electron Beam Accelerator Facility.

**CERN** European Organization for Nuclear Research.

**CMS** Compact Muon Solenoid.

**ECal** Electromagnetic Calorimeter.

**FT-Cal** Forward Tagger Calorimeter.

**HEAT** High Energy Antimatter Telescope.

**HPS** Heavy Photon Search.

**HV** High Voltage.

**IC** Inner Calorimeter.

**JLab** Thomas Jefferson National Accelerator Facility.

**LED** Light Emitting Diode.

**LMS** Light Monitoring System.

**PAMELA** Payload for Antimatter Exploration and Light-nuclei Astrophysics.

**PCBs** Printed Circuit Boards.

**Phenix** Pioneering High Energy Nuclear Interaction eXperiment.

**QED** Quantum Electrodynamics.

**SICCAS** Shanghai Institute of Ceramics, Chinese Academy of Sciences.

**SM** Standard Model.

**SVT** Silicon Vertex Tracker.

**WIMPs** Weakly Interacting Massive Particles.

**WMAP** Wilkinson Microwave Anisotropy Probe.

# Bibliography


[1] B. Holdom. *Physics Letters B*, **178**:65-710, 1986.

[2] O. Adriani et al. *Nature*, **458**:607-609, 2009.

[3] J. Chang et al. *Nature*, **456**:362-365, 2008.

[4] J.A. Jaros et al. *Heavy Photon Search Experiment at Jefferson Laboratory: proposal for run 2014-2015*, Internal Report, 2013.

[5] R.-Y. Zhu. *Radiation Damage Effects, Handbook of Particle Detection and Imaging*, Springer Reference, 2012.

[6] P. Rosier. *Deeply Virtual Compton Scattering Experiment Inner calorimeter*, IPN Orsay - Internal Report, 2004.

[7] F. Zwicky. *Helvetica Physica Acta*, **6**:110127, 1933.

[8] K.G Begeman. *Astron. Astrophysics*, **223**:47-60, 1989.

[9] G. Jungman et al. *Phys. Rept. Lett.*, **267**:195-373, 1996.

[10] W. Buchamuller et al. *JHEP*, **703**:37, 2007.

[11] N. Arkani-Hamed et al. *Phys. Rev. Lett.*, **D79**:015014, 2009.

[12] J. D. Bjorken et al. *Phys. Rev. Lett.*, **D80**:075018, 2009.

[13] M. Goodsell et al. *JHEP*, **911**:27, 2009.

[14] D.P. Finkbeiner et al. *JCAP* , **1105**:2, 2011.

[15] P. Picozza et al. *Astropart. Phys.*, **27**:296-315, 2007.

[16] I. Cholis et al. *Phys. Rev. Lett*, **D80**:123518, 2009.

[17] E. Komatsu et al. *Astrophys. J. Suppl.*, **192**:18, 2011.

[18] A. Adare et al. *eprint*, arXiv:1409.0851, 2014.

[19] H. Merkel et al. *Phys. Rev. Lett.*, **112**:221802, 2014.

[20] J.A. Jaros et al. *A proposal to Search for Massive Photons at Jefferson Laboratory*, Internal Report, 2010.

[21] C W. Leemann et al. *Anne. Rev. Nucl. Part Sci.*, **51**:413-50, 2001.

[22] M. Contalbrigo et al. *Nucl. Instr. Meth, Phys. Res.*, **A639**:302306, 2011.

[23] T.K. Nelson. *Proceedings of Science, 21st International Workshop on Vertex Detectors*, Conference Note, 2012.

[24] CMS Experiment. *CERN/LHCC*, 97-33, 1997.

[25] L.Y. Zhang et al. *IEEE Transaction on Nuclear Science*, **48**:3, 2001.

[26] The CMS ECAL Group. *JINST*, **5**:P03010, 2010.

[27] G F. Knoll *Radiation Detection and Measurement*, Third edition book, 1991.

[28] The ALICE Experiment. *JINST*, **3**:S08002, 2008.

[29] V.A. Batarin et al. *Instruments and Experimental Techniques*, 46:753-757, 2003.

[30] V.Dormenev, et.al. *Nucl. Instr. Meth, Phys. Res.*, **365**:291, 1995.

[31] The PANDA Collaboration. *TDR for PANDA (EMC)*, arXiv:0810.1216, 2008.

[32] CLAS12 Collaboration. *CLAS12 Forward Tagger (FT) Technical Design Report*, Internal Report, 2012.

[33] A.Rizzo etal. *LAAPD benchmarking: Activity Report*, Internal Report, 2014.

[34] L. M. P Fernandes et al. *IEEE Transactions on Nuclear Science*, **51**:4, 2004.

[35] Hamamatsu. *Technical information characteristics and use of Si APD*, Manufactures Guide.

[36] Hamamatsu. *Si APD (Avalanche Photodiode)*, Manufactures Guide.

[37] Tru-Opto. *Bi-coloured LEDs, 5mm Red & Blue LED*, Manufactures Guide.

[38] V. A. Batarin etal. *Nucl. Instrum. Meth. Phys. Res.*, **A556**:94-99, 2006.

[39] Agilent Technologies. *Agilent Cary 4000/5000/6000i Series UV-VIS-NIR Spectrophotometers*, Manufactures Guide.

[40] P. Lecoq et al. Nucl.Instrum.Meth.Phys.Res., **A365**:297-298, 1995.

[41] J. Wu et al. *Nucl. Instrum. Meth. Phys. Res.*, **A404**:311-314, 1998.

[42] ROHM Semiconductor, *LED Fundamentals*, Manufacturers Guide.